



HAL
open science

Boundary Element Modeling of Two-Plate Interaction at Subduction Zones: Scaling Laws and Application to the Aleutian Subduction Zone

G. Gerardi, Neil M. Ribe

► **To cite this version:**

G. Gerardi, Neil M. Ribe. Boundary Element Modeling of Two-Plate Interaction at Subduction Zones: Scaling Laws and Application to the Aleutian Subduction Zone. *Journal of Geophysical Research: Solid Earth*, 2018, 123 (6), pp.5227-5248. 10.1002/2017JB015148 . hal-01968775

HAL Id: hal-01968775

<https://hal.science/hal-01968775>

Submitted on 3 Jan 2019

HAL is a multi-disciplinary open access archive for the deposit and dissemination of scientific research documents, whether they are published or not. The documents may come from teaching and research institutions in France or abroad, or from public or private research centers.

L'archive ouverte pluridisciplinaire **HAL**, est destinée au dépôt et à la diffusion de documents scientifiques de niveau recherche, publiés ou non, émanant des établissements d'enseignement et de recherche français ou étrangers, des laboratoires publics ou privés.

Boundary-element modeling of two-plate interaction at subduction zones: scaling laws and application to the Aleutian subduction zone

G. Gerardi¹ and Neil M. Ribe¹

¹FAST, Univ Paris-Sud/CNRS, 23-25 rue Jean Rostand, Parc Club Orsay Université, F-91405 Orsay.

Key Points:

- The subduction interface strength strongly affects the kinematics of the subducting plate. The plate speed depends logarithmically on the plate length
 - Overriding plate deformation occurs by a combination of extension/compression and bending. Back-arc extension is observed only for a positively buoyant overriding plate
 - We estimate an interface viscosity $\eta_{SI} = (0.96-1.72) \times 10^{20}$ Pa s for the central Aleutian subduction zone
-

Corresponding author: G. Gerardi, gianluca.gerardi@u-psud.fr

Abstract

This work uses the boundary-element method (BEM) to explore the dynamics of subduction of a dense lithospheric plate (subducting plate, SP) beneath an overriding plate (OP). For simplicity, the model is two-dimensional, the plates are purely viscous, and the ambient fluid is infinitely deep. The negative buoyancy of the slab is the only driving force of the system. First, we study the SP kinematics focusing on two characteristic instantaneous velocities: the convergence speed (V_{Conv}) of the descending slab and the horizontal plate speed (U_{SP}) of the flat portion of the SP. We find that V_{Conv} is entirely controlled by the slab's geometry, by the width of the lubrication layer d_2 separating the SP and the OP and by the SP's flexural stiffness St . Turning to U_{SP} , we find that this parameter depends not only on d_2 and St , but also on the lengths L_{SP} and L_{OP} of the two plates. The dependence of U_{SP} on L_{SP} is exactly logarithmic, both with and without an OP. Next, we explore the deformation of the OP, which occurs by a combination of extension/compression and bending. The OP deformation is compression-dominated close to the trench and bending-dominated along the remaining portion of the OP that undergoes significant deformation. For a positively buoyant OP, back-arc extension is also observed. Finally, we estimate the subduction interface viscosity η_{SI} of the central Aleutian subduction zone, running our BEM model with the appropriate geometry according to Lallemand *et al.* [2005]. We find $\eta_{\text{SI}} = (0.96 - 1.72) \times 10^{20}$ Pa s.

1 Introduction

Understanding the subduction of a dense lithospheric plate (subducting plate, SP) beneath an overriding plate (OP) is a major challenge in current geodynamics. Although this phenomenon represents one of the main ingredients of global-scale mantle convection, various aspects of it remain to be clarified.

As a preliminary, we note that much progress in our understanding of subduction has come from models that consider an isolated SP without an OP. In particular, this approach has provided insight into the origin of the different modes of subduction that have been observed in both analog and numerical models. A number of recent studies have shown that the viscosity contrast ($\lambda \equiv \eta_1/\eta_0$) between the SP (η_1) and the surrounding mantle (η_0) is one of the key parameters controlling the different styles of subduction [Kincaid & Olson, 1987; Di Giuseppe *et al.*, 2008; Schellart, 2010]. On the basis of laboratory experiments, Funicello *et al.* [2008], identified two critical ranges of λ that delimit two styles of subduction: $\lambda \gg 10^4$ where subduction always occurs in the so-called 'trench-retreating' mode, and $10^2 \leq \lambda \leq 10^4$ where both trench-retreating and trench-advancing modes are observed depending on the geometry and the buoyancy of the SP. According to Bellahsen *et al.* [2005], narrow, thin and heavy plates tend to subduct in trench-retreating mode, while wide, thick and light plates prefer the trench-advancing mode. A more detailed phase diagram was proposed by Schellart [2008a] in terms of λ and the ratio D/h between the depth D of the mantle layer and the SP thickness h . Using both these parameters, the author was able to classify a broad range of data from different laboratory studies [Bellahsen *et al.*, 2005; Funicello *et al.*, 2006; Schellart, 2004]. He identified four main modes of subduction: 1) trench retreating at low λ ; 2) slab folding, 3) trench-advancing, and 4) trench-retreating at high λ . The same phase diagram was reproduced qualitatively by Ribe [2010] using a 2-D boundary-element (BEM) numerical model and quantitatively by Li & Ribe [2012] using a 3-D BEM model. They found that the boundaries separating the different modes reported by Schellart [2008a] are the contour lines of the function $\theta_D = \text{fct}(\lambda, D/h)$, where θ_D is the dip of the subducting slab as it impinges on the base of the experimental tank (a rough analog of the 660 km dis-

continuity). Ribe [2010] and Li & Ribe [2012] also clarified the role of λ in the dynamics of the SP by identifying a key dimensionless parameter, the SP's 'flexural stiffness' $St \equiv \lambda (h/\ell_b)^3$, where ℓ_b is the length of the portion of the SP where the deformation is dominated by bending. They showed that the slab's sinking speed V_{Sink} is controlled by the ambient mantle viscosity η_0 when $St \leq 1$, and by the SP viscosity η_1 when $St \gg 1$.

However, even if models of an isolated SP are useful to capture meaningful features of subduction, adding an OP to the system appears crucial for more realistic modeling of natural subduction zones. In this context three main questions arise: i) how does the presence of the OP influence the kinematics of the SP? ii) what controls the interplate stress state along the subduction interface? iii) what drives the deformation and motion of the OP [Schellart, 2008b; van Dinther *et al.*, 2010; Duarte *et al.*, 2013; Garel *et al.*, 2014; Holt *et al.*, 2015; Krien & Fleitout, 2008; Butterworth *et al.*, 2012]?

As for the case of an isolated SP, both 'forced' and 'free' systems have been widely used for analog and numerical modeling of subduction with an OP. In the first (forced) case, the model is partially or totally forced by a boundary condition imposed as a kinematic constraint. Commonly, the subduction rate of the SP is imposed, either with a piston that pushes the SP toward the OP in analog models [e.g. Shemenda, 1993] or by prescribing it as a boundary condition in numerical models [e.g. Rodríguez-González *et al.*, 2012; He, 2012]. This approach is useful to study specific features of subduction, and also when one wants to mimic the effect of far-field driving forces [Schellart & Strak, 2016]. However, it lacks self-consistency since there is an external source that continuously adds energy to the system. In the second (free) case, the motion and deformation of the plates are controlled entirely by the internal forces in the system. Usually, the only driving force taken into account is slab pull since ridge push is one order of magnitude smaller [Turcotte & Schubert, 2002]. This type of approach is useful for understanding the natural evolution of subduction systems and the causal link between the forces and the velocities observed within them.

In recent years, several authors have used 3-D analog and numerical models of the free class to address the question of the mechanism of deformation of the OP, focussing in particular on the controlling factor for back-arc extension. In general, it is found that back-arc extension is strongly correlated with trench retreat [Meyer & Schellart, 2013; Schellart & Moresi, 2013; Duarte *et al.*, 2013; Chen *et al.*, 2016]. A possible mechanical interpretation of this result is that slab rollback induces a toroidal mantle flow that exerts shear stresses on the base of the OP that in turn lead to back-arc opening. The rate of extension in the back-arc zone depends on whether the OP is free to move or is fixed at its end on the opposite side from the trench [Chen *et al.*, 2015]. Interestingly, back-arc extension is also observed in the 2-D (toroidal flow absent by definition) numerical model of Holt *et al.* [2015] when the OP is positively buoyant. For such a case, if the poloidal flow suddenly becomes weaker due to interaction of the slab with a viscosity increase at 660 km depth, a shift from extension to compression in the back-arc zone may occur.

Another feature that has been explored recently is the influence of the subduction interface on the deformation of the OP and the rate of subduction of the SP. Based on analog models, Duarte *et al.* [2013] and Chen *et al.* [2015] concluded that interplate stresses at the interface are the primary control on forearc deformation within the OP. The forearc can be compressional or extensional depending on the magnitude of those stresses, whereas backarc deformation is insensitive to them. Duarte *et al.* [2013] also found that the subduction rate of the SP is controlled by the rheology of the subduction interface, decreasing strongly as the viscosity of the interface increases due to enhanced mechanical coupling between the plates.

Turning finally to the influence of the OP on the kinematics of the SP, Holt *et al.* [2015] showed that the OP viscosity does not influence significantly any of the characteristic velocities of the SP. They also found that increasing the OP's thickness decreases the

rate of slab rollback, but does not affect the subduction rate or the slab's sinking speed. The same correlation between trench motion and the thickness of the OP is also found in the 2-D numerical model of Garel *et al.* [2014]. By systematically varying the ages (i.e., the thicknesses) of both plates and following the time evolution of subduction in a viscosity-stratified mantle, Garel *et al.* [2014] were able to determine a phase diagram that reproduces a wide range of deep slab morphologies observed in nature.

Despite the impressive recent progress in modeling SP/OP interaction, a full picture that can convincingly describe the underlying mechanics is still missing. Here we endeavor to shed light on this problem using a 2-D numerical model of free subduction in which a SP and an OP interact across a relatively weak interface. Our work differs from previous numerical approaches in several ways. First and most importantly, we treat the subduction interface strength as a variable parameter and explore its influence systematically, whereas most previous numerical models treat it as constant [e.g. van Hunen *et al.*, 2000; Babeyko & Sobolev, 2008; Bottrill *et al.*, 2012; Rodríguez-González *et al.*, 2012; Holt *et al.*, 2015]. Second, we focus on the determination of quantitative scaling laws that express relations among key dimensionless parameters characterizing the system. Third, we systematically employ concepts of thin viscous-sheet theory to interpret our results. Finally, we solve the model equations using a somewhat unusual numerical technique, the BEM, whose considerable advantages are described in § 3.

The outline of the paper is as follows. After introducing the model setup and the BEM, we set the stage with an overview of time-dependent subduction without and with an OP. This section makes clear the critical influence of the subduction interface strength. Next, we exploit the quasi-static character of Stokes flow to examine instantaneous solutions of the model equations, for both the SP ONLY and the SP+OP cases. A key result here is that the surface speed of the SP always depends logarithmically on the ratio of the surface plate length to the slab length. We also determine a scaling law for the convergence rate as a function of the flexural stiffness of the SP and the dimensionless subduction interface thickness. We then turn to an analysis of the deformation state of the OP, using instantaneous BEM solutions interpreted in terms of thin viscous-sheet theory. These solutions show that the deformation of the OP is dominated by compression, bending, and (in some cases) extension as one moves from the forearc to the backarc region. Finally, we apply our results by using BEM solutions with realistic geometry to infer the long-term strength of the subduction interface in the central Aleutian subduction zone.

2 Model

Figure 1 shows the initial configuration ($t = 0$) of the model, and table 1 summarizes the notation adopted. The domain is 2D, infinitely deep and bounded at $x_2 = 0$ by a free-slip surface (i.e. impermeable and free of shear traction). Two thin sheets are immersed in the ambient fluid half-space. Their cross-sectional areas are S_1, S_2 and their interfacial contours are C_1, C_2 , respectively, where the subscript 1 represents the SP and 2 the OP.

The viscosity of the SP is $\eta_1 = \lambda_1 \eta_0$, where η_0 is the ambient fluid viscosity. Its density is $\rho_1 = \rho_0 + \Delta\rho_1$, where ρ_0 is the ambient fluid density and $\Delta\rho_1 > 0$ is the density excess of the SP relative to the ambient fluid. The viscosity of the OP is $\lambda_2\eta_0$ and its density ρ_2 can be equal or smaller than ρ_0 , depending on whether the OP is neutrally or positively buoyant, respectively.

The SP comprises a flat portion of length L_{SP} and a bent piece (the slab) of length ℓ whose leading end subducts with an initial angle θ_0 . The plate has a constant thickness h_{SP} except for the two rounded ends. The SP's midsurface lies halfway between its upper and lower surfaces, and the arclength coordinate along the midsurface is $s \in [0, L_{SP} + \ell]$. At $t = 0$, the shape of the slab's midsurface is analytically specified by its dip $\theta(s)$, given by

$$\theta(s) = \theta_0 \hat{s}^2 (3\ell - 2\hat{s}) / \ell^3 \quad (1)$$

where $\hat{s} = s - L_{SP}$. Eq. (1) ensures that the midsurface curvature $K(s) = -d\theta/ds$ is initially zero at both $s = L_{SP}$ and $s = L_{SP} + \ell$.

The OP comprises at $t = 0$ a central flat portion with constant thickness h_{OP} and length L_{OP} , bounded on the right by a rounded end and on the left by a triangular portion separated from the SP by a gap (lubrication layer) of constant width d_2 . The exact shape of the triangular piece depends on the choice of ℓ and d_2 . Sharp corners that could reduce the accuracy of the numerical method are avoided by rounding two of the corners of the triangular piece. The arclength coordinate on the OP's midsurface is $s_{OP} \in [0, L_{OP}]$.

Referring again to figure 1, we point out that another lubrication layer of thickness d_1 is present above the SP and the OP. Its role is to allow an 'earthlike' lateral movement of the plates. According to lubrication theory, strong normal stresses develop in the thin layer and resist the vertical motion of the plates when they are subjected to a vertical force. In the case of the negatively buoyant SP, an upward-directed normal stress $\sim h_{SP}g\Delta\rho_1$ is set up in the layer and exactly compensates the negative buoyancy of the flat portion of the plate, which is then free to move laterally in response to slab pull [Ribe, 2010]. The situation is opposite for a positively buoyant OP: downward-directed normal stresses $\sim h_{OP}g\Delta\rho_2$ prevent the OP from rising towards the free-slip surface, and allow it to deform freely in response to its buoyancy and the influence of the nearby slab.

3 BEM formulation

Because inertia is negligible in the mantle, the flow within the plates and outside them is governed by the Stokes equation of motion. Stokes flow problems with deformable fluid/fluid interfaces can be efficiently solved using the boundary-element method (BEM). This numerical technique is based on the boundary-integral representation of Stokes flow, whereby the flow in a given domain is expressed in terms of weighted integrals of the tractions and velocities on the boundaries of the domain. The method is especially well adapted to tracking fluid-fluid interfaces having continuous curvature, like the ones shown in figure 1. The BEM has several advantages: unwanted wall effects are entirely absent, the dimensionality of the problem is reduced by one (from 2-D to 1-D in our case), and it is easy to obtain high (fourth-order) accuracy of the solutions for the velocity at each time step.

The model problem sketched in figure 1 comprises three distinct fluid regions, two of which are singly connected. For this geometry, the boundary-integral representation allows one to derive the following integral equation for the flow field [Manga & Stone, 1993; Pozrikidis, 1992]:

$$\begin{aligned} \chi_0(\mathbf{x})\mathbf{u}^{(0)}(\mathbf{x}) + \chi_1(\mathbf{x})\lambda_1\mathbf{u}^{(1)}(\mathbf{x}) + \chi_2(\mathbf{x})\lambda_2\mathbf{u}^{(2)}(\mathbf{x}) = \\ = \frac{\Delta\rho_1}{\eta_0} \int_{C_1} (\mathbf{g} \cdot \mathbf{y})\mathbf{n}(\mathbf{y}) \cdot \mathbf{J}(\mathbf{y} - \mathbf{x})d\mathbf{l}(\mathbf{y}) + \frac{\Delta\rho_2}{\eta_0} \int_{C_2} (\mathbf{g} \cdot \mathbf{y})\mathbf{n}(\mathbf{y}) \cdot \mathbf{J}(\mathbf{y} - \mathbf{x})d\mathbf{l}(\mathbf{y}) + \\ + (1 - \lambda_1) \int_{C_1} \mathbf{u}^{(1)}(\mathbf{y}) \cdot \mathbf{K}(\mathbf{y} - \mathbf{x}) \cdot \mathbf{n}(\mathbf{y}) d\mathbf{l}(\mathbf{y}) + (1 - \lambda_2) \int_{C_2} \mathbf{u}^{(2)}(\mathbf{y}) \cdot \mathbf{K}(\mathbf{y} - \mathbf{x}) \cdot \mathbf{n}(\mathbf{y}) d\mathbf{l}(\mathbf{y}). \end{aligned} \quad (2)$$

In (2), $\mathbf{u}^{(i)}(\mathbf{x})$ ($i = 0, 1$ or 2) is the velocity of the fluid at the point $\mathbf{x} \in S_i$. The density differences are $\Delta\rho_i = (\rho_i - \rho_0)$, and $\mathbf{n}(\mathbf{y})$ is the unit vector normal to the contour that points out of the plates. The coefficients $\chi_i(\mathbf{x})$ for $i = 1$ and 2 have the values $0, 1/2$ or 1 if $\mathbf{x} \notin S_i$, $\mathbf{x} \in C_i$ or $\mathbf{x} \in S_i$, respectively. The coefficient $\chi_0(\mathbf{x})$ is 0 for $\mathbf{x} \notin S_0$, $1/2$ for $\mathbf{x} \in C_1 \vee \mathbf{x} \in C_2$ and 1 for $\mathbf{x} \in S_0$. $\mathbf{J}(\mathbf{y} - \mathbf{x})$ and $\mathbf{K}(\mathbf{y} - \mathbf{x})$ are Green's functions that represent singular solutions of the Stokes equation for the velocity and the stress, respectively, at the point \mathbf{y} due to a line force at \mathbf{x} . In order to satisfy the free-slip condition at $x_2 = 0$, they are defined as:

$$J_{ij}(\mathbf{y} - \mathbf{x}) = J_{ij}^*(\mathbf{y} - \mathbf{x}) + (-1)^{j+1} J_{ij}^*(\mathbf{y} - \mathbf{x}^{\text{IM}}) \quad (3)$$

$$K_{ijk}(\mathbf{y} - \mathbf{x}) = K_{ijk}^*(\mathbf{y} - \mathbf{x}) + (-1)^{j+1} K_{ijk}^*(\mathbf{y} - \mathbf{x}^{\text{IM}}) \quad (4)$$

where $\mathbf{x}^{\text{IM}} \equiv \mathbf{x} - 2x_2\mathbf{e}_2$ is the mirror image of the point \mathbf{x} across the boundary $x_2 = 0$ and

$$J_{ij}^*(\mathbf{r}) = \frac{1}{4\pi} \left(-\delta_{ij} \ln|\mathbf{r}| + \frac{r_i r_j}{|\mathbf{r}|^2} \right), \quad K_{ijk}^*(\mathbf{r}) = -\frac{1}{\pi} \left(\frac{r_i r_j r_k}{|\mathbf{r}|^4} \right) \quad (5)$$

are the Green's functions for a line force in an infinite fluid.

Adopting the dimensionless (hatted) variables

$$(\hat{\mathbf{x}}, \hat{\mathbf{y}}) = h_{\text{SP}}^{-1}(\mathbf{x}, \mathbf{y}), \quad \hat{\mathbf{u}}^{(i)} = \frac{\eta_0}{h_{\text{SP}}^2 \Delta\rho_1} \mathbf{u}^{(i)} \quad (i = 1, 2) \quad (6)$$

and then suppressing the hats to simplify the notation, we may write the dimensionless form of eq.(2) as

$$\begin{aligned} \int_{C_1} -(\mathbf{e}_2 \cdot \mathbf{y})\mathbf{n} \cdot \mathbf{J}d\mathbf{l} - \Gamma \int_{C_2} (\mathbf{e}_2 \cdot \mathbf{y})\mathbf{n} \cdot \mathbf{J}d\mathbf{l} + (1 - \lambda_1) \int_{C_1} \mathbf{u}^{(1)} \cdot \mathbf{K} \cdot \mathbf{n}d\mathbf{l} + \\ + (1 - \lambda_2) \int_{C_2} \mathbf{u}^{(2)} \cdot \mathbf{K} \cdot \mathbf{n}d\mathbf{l} = \begin{cases} \mathbf{u}^{(0)}(\mathbf{x}) & \text{if } \mathbf{x} \in S_0 \\ \lambda_1 \mathbf{u}^{(1)}(\mathbf{x}) & \text{if } \mathbf{x} \in S_1 \\ \lambda_2 \mathbf{u}^{(2)}(\mathbf{x}) & \text{if } \mathbf{x} \in S_2 \\ (1 + \lambda_1)/2 \mathbf{u}^{(1)}(\mathbf{x}) & \text{if } \mathbf{x} \in C_1 \\ (1 + \lambda_2)/2 \mathbf{u}^{(2)}(\mathbf{x}) & \text{if } \mathbf{x} \in C_2 \end{cases} \end{aligned} \quad (7)$$

where $\mathbf{e}_2 = -\mathbf{g}/g$ is the (upward-pointing) vertical unit vector, $\Gamma \equiv \Delta\rho_2/\Delta\rho_1$, and the arguments of \mathbf{u} , \mathbf{n} , \mathbf{J} , \mathbf{K} and dl have been suppressed to simplify the notation.

Equations (7) allow for a complete calculation of the flow field in the whole space domain. The first step is to consider points $\mathbf{x} \in C_1$ and $\mathbf{x} \in C_2$, for which (7) reduces to a pair of coupled Fredholm integral equations of the second kind for the interfacial velocities of the plates. Then, once $\mathbf{u}^{(1)}$ and $\mathbf{u}^{(2)}$ on the surfaces of the plates are known, the velocity within the plates or in the ambient fluid can be determined by solving the equations of (7) for the regions of interest. Finally, if we are interested also in time dependent solutions, we can advance in time the material points $\mathbf{x} \in C_1$ and $\mathbf{x} \in C_2$ according to:

$$\frac{d\mathbf{x}}{dt} = \mathbf{u}(\mathbf{x}) \quad (8)$$

where the dimensionless time is

$$\hat{t} = \frac{h_{SP}g\Delta\rho_1}{\eta_0}t. \quad (9)$$

The numerical solution procedure adopted for the solution of (7) when $\mathbf{x} \in C_1$ and $\mathbf{x} \in C_2$ consists of the following steps. First, the integrals are regularized by subtracting the singularity at $\mathbf{y} = \mathbf{x}$ [Pozrikidis, 1992], which yields:

$$\int_{C_i} (\mathbf{e}_2 \cdot \mathbf{y}) \mathbf{n} \cdot \mathbf{J} dl = \int_{C_i} \mathbf{e}_2 \cdot (\mathbf{y} - \mathbf{x}) \mathbf{n} \cdot \mathbf{J} dl \quad (10)$$

$$\int_{C_i} \mathbf{u}^{(i)}(\mathbf{y}) \cdot \mathbf{K} \cdot \mathbf{n} dl = \int_{C_i} [\mathbf{u}^{(i)}(\mathbf{y}) - \mathbf{u}^{(i)}(\mathbf{x})] \cdot \mathbf{K} \cdot \mathbf{n} dl - \frac{1}{2} \mathbf{u}^{(i)}(\mathbf{x}) \quad (11)$$

where $i = 1$ and 2 . Next, the contours C_1 and C_2 are discretized using three-node curved elements C_{n_1} ($n_1 = 1, 2, \dots, N_1$) and C_{n_2} ($n_2 = 1, 2, \dots, N_2$), over each of which \mathbf{y} , \mathbf{n} and \mathbf{u} vary as

$$\begin{aligned} \mathbf{y}(\xi) &= \sum_{m=1}^3 \phi_m(\xi) \mathbf{y}_m, & \mathbf{n}(\xi) &= \frac{\partial_\xi \mathbf{y} \times \mathbf{e}_3}{|\partial_\xi \mathbf{y} \times \mathbf{e}_3|}, \\ \mathbf{u}(\xi) &= \sum_{m=1}^3 \phi_m(\xi) \mathbf{u}_m, \end{aligned} \quad (12)$$

where \mathbf{y}_m are the (known) nodal coordinates, \mathbf{u}_m are the (unknown) nodal velocities and $\phi_m(\xi)$ are quadratic basis functions defined on a master element $\xi \in [-1, 1]$. Substitution of (12) into (7) transforms the integrals over C_1 and C_2 into sums over the elements C_{n_1} and C_{n_2} , each of which is evaluated on $\xi \in [-1, 1]$ using 6-point Gauss-Legendre quadrature. The resulting system of $4(N_1 + N_2)$ coupled linear equations is solved iteratively using the biconjugate gradient algorithm of Press *et al.* [1992], yielding the nodal velocities \mathbf{u}_m with fourth-order-accuracy. Finally, the evolution in time of the shape of the plates is obtained by solving (8) with a second-order Runge-Kutta (midpoint) method.

We emphasize that the element size (mesh resolution) is variable along the two contours, being smaller along the portions that adjoin the thin lubrication layers. This is done in order to avoid the loss of numerical accuracy that occurs when the distance between the observation point \mathbf{y} and the source point \mathbf{x} of the Green's functions is smaller than the element size (see Appendix C: for more details).

To test the accuracy of the model, we ran simulations for a geometry comprising two effectively solid ($\lambda_1 = \lambda_2 = 10^5$) cylinders of radius R with $\Gamma = 1$, located at the same depth and separated by a horizontal distance d_2 . We computed the horizontal (u_1) and vertical (u_2) components of the velocity of the cylinders as well as their spin ω , as functions of increasing d_2 . In the limit $d_2/R \gg 1$, $u_1 \rightarrow 0$ and $\omega \rightarrow 0$, and u_2 approaches the prediction of the analytical solution of Wakiya [1975] for a solid cylinder sinking normal to a free-slip surface (figure provided by the authors upon request).

4 Unsteady subduction

We begin our study with an overview of the qualitative features of the temporal evolution of the system. For reference, we first examine the unsteady subduction of an isolated SP (from now on the SP ONLY case), adding the OP later to see how its presence influences the dynamics. We shall refer to the latter case as the SP+OP case.

Figure 2 shows the initial and final states of three simulations starting from initial configurations given in table 2. Figure 2a shows the subduction of an isolated SP to $\hat{t} = 21.5$, at which time the slab's tip is at a depth $6.8h_{\text{SP}}$ (corresponding to a dimensional depth 660 km for $h_{\text{SP}} = 100$ km and $d_1/h_{\text{SP}} = 0.2$.) We then add the OP and run the simulation for the same dimensionless time $\hat{t} = 21.5$. The cases shown in figs. 2b and 2c differ only in the thickness d_2 of the lubrication layer between the plates, which is $0.2h_{\text{SP}}$ for the former case and $0.08h_{\text{SP}}$ for the latter.

Comparing the SP ONLY case and both SP+OP cases, we immediately see that the presence of the OP leads to an overall slowing down of the subduction process, as indicated by the reduced convergence rate and trench rollback speed. Moreover, the slowing-down is more pronounced for the smaller lubrication gap thickness. This is indicated by the depths reached by the slabs at $\hat{t} = 21.5$, which are 340 km for $d_2/h_{\text{SP}}=0.2$ and 275 km for $d_2/h_{\text{SP}}=0.08$. Furthermore, the OP moves seaward as subduction proceeds, indicating the strong mechanical coupling of the OP and the SP across the lubrication gap separating them.

A useful parameter for illustrating the evolution of subduction is the length ℓ_s of the sheet's midsurface that is below the depth $x_2 = -h_{\text{SP}} - d_1$ of the base of the plate. The derivative $d\ell_s/dt$ is then the instantaneous convergence rate. Figure 3(a) shows $\hat{\ell}_s = \ell_s/h_{\text{SP}}$ for the three cases of figure 2. The convergence rate is an increasing function of d_2 at all times. This reflects the influence of the viscous drag exerted on the SP by the subduction interface, which increases as d_2 decreases for a given magnitude of the relative tangential velocity between the SP and the OP. The subduction interface drag force works against the slab pull, leading to slower subduction. This effect is emphasized in figure 3b, which shows the instantaneous convergence rate $(d\ell_s/dt)_{t=0}$ at the initial time as a function of the dimensionless thickness of the subduction interface. The convergence rate strongly decreases as the subduction interface becomes thinner.

The dominant role of the parameter d_2/h_{SP} becomes even clearer if we examine the influence of the geometry and physical properties of the OP on the evolution of ℓ_s . To do so, we fix $d_2/h_{\text{SP}} = 0.2$ and we explore individually the effects of the OP length $L_{\text{OP}}/h_{\text{SP}} \in [8 - 32]$, its thickness $h_{\text{OP}}/h_{\text{SP}} \in [0.75 - 1.25]$, its viscosity $\lambda_2 \in [150 - 600]$ and its density $\Gamma \in [-0.5 - 0]$. It turns out that all the different curves $\ell_s(t)$ remain identical to the one depicted in fig. 3(a), thus proving that none of the OP properties listed above have any influence on the convergence rate. Only the thickness h_{OP} shows a certain effect for long times ($\hat{t} \geq 10$), with a higher value of h_{OP} resulting in a lower value of the subducted length $\hat{\ell}_s$ and vice versa (figure provided by the author upon request). However, this variation is small (2-3%) compared to the effect of varying d_2/h_{SP} , which is therefore the dominant parameter controlling $\ell_s(t)$.

To conclude this section, we highlight an interesting feature of the geometry of the lubrication gap at the end of our SP+OP simulations. While the gap initially has a constant thickness d_2 , it evolves during subduction so that it is narrower at the bottom than at the top (inset of 2c). This aspect is quantified in figure 4 where we track the time evolution of the maximum (d_2^{max}) and minimum (d_2^{min}) thickness of the subduction interface for the model of fig. 2c. The lubrication layer quickly widens at the top (increasing d_2^{max}) while thinning at the bottom (decreasing d_2^{min}). This means that subduction of the SP drags fluid from the wider to the narrower part of the gap. According to lubrication

theory, this is precisely the condition required to build up a positive excess pressure in the gap that keeps the two plates apart.

5 Thin-sheet analysis: SP kinematics

We begin by recalling the property of instantaneity of slow viscous flow with negligible inertia. A consequence of this property is that the dynamics of the two interacting plates are entirely determined at each instant by the geometry of the system at that instant and by the fluid properties (i.e. density and viscosity of the ambient fluid and of the plates). Thus, in order to study the mechanics of SP-OP interaction it makes sense first to examine quasi-static configurations, without the added complexity of the purely kinematic time evolution. Following this approach, in this section and in § 6 we shall refer only to instantaneous solutions of the model (eq. (7)) whose geometrical parameters (e.g. θ_0 , ℓ , L_{SP} , h_{OP} etc.) will be varied in order to represent different subduction zones at some arbitrary instant in time.

In order to better highlight the effect of the OP, we first review the case of free subduction of an isolated SP, recalling existing results and obtaining some new ones.

5.1 Instantaneous solutions: SP only

The crucial dimensionless parameter that controls the free subduction of an isolated SP can be determined using a simple scaling analysis of the forces acting on the portion of the SP that deforms by bending [Ribe, 2010]. The analysis is carried out for a subducting plate whose leading end dips at an angle θ_0 and sinks with a vertical velocity V_{Sink} . Three forces act on the bending portion of the plate: the negative buoyancy of the slab, the internal viscous resistance to bending, and the traction applied by the external fluid. Balancing the negative buoyancy and the external traction yields a typical sinking speed $V_{\text{Sink}} \sim V_{\text{Stokes}}$, where

$$V_{\text{Stokes}} = \frac{h_{\text{SP}} \ell g \Delta \rho_1}{\eta_0}. \quad (13)$$

The characteristic ratio of the internal viscous resistance to the external traction is the ‘flexural stiffness’

$$\text{St} = \frac{\eta_1}{\eta_0} \left(\frac{h_{\text{SP}}}{\ell_b} \right)^3, \quad (14)$$

where ℓ_b is the ‘bending length’, defined as the distance from the leading end of the SP’s midsurface to one characteristic zero of the function $K(s)$ that quantifies the rate of curling of the SP’s midsurface. See figure 5 of Ribe [2010] for details. In geodynamical terms, ℓ_b is the sum of the slab length and the length of the region seaward of the trench where flexural bulging occurs. Ribe [2010] showed that the sinking speed V_{Sink} obeys a scaling law of the form

$$\frac{V_{\text{Sink}}}{V_{\text{Stokes}}} = \text{fct}(\text{St}, \theta_0), \quad (15)$$

which states that two SPs are dynamically similar if they have the same values of St and θ_0 . The requirement that θ_0 be the same for both SPs is the condition for geometrical similarity of the slab’s midsurface. Numerical solutions [Ribe, 2010] show that V_{Sink} does not depend on L_{SP} , which implies that geometrical similarity of the midsurface of the whole plate is not required.

As an illustration of the scaling law (15), fig. 5 shows $V_{\text{Sink}}/V_{\text{Stokes}}$ vs. St for $\theta_0 = 30^\circ$, obtained from BEM solutions for different values of d_1/h_{SP} , ℓ/h_{SP} , and η_1/η_0 . All the points collapse onto a single master curve, validating (15). The master curve has two distinct limits. In the ‘Stokes’ limit $\text{St} \leq 1$, the slab’s negative buoyancy is balanced by the external traction. The slope of the curve is zero, meaning that the sinking speed is controlled entirely by the viscosity η_0 of the ambient fluid. In the ‘flexural’ limit $\text{St} \gg 1$, by contrast, the negative buoyancy is balanced by the internal resistance to bending. The slope of the curve is -1 , and the sinking speed is controlled by the viscosity η_1 of the SP.

With the definition of St in hand, we now determine a scaling law for the plate speed U_{SP} , defined as the average horizontal velocity of the midsurface of the flat por-

tion of the SP. Unlike V_{Sink} , U_{SP} depends on the plate length L_{SP} , because a longer plate is subject to a greater drag force from the underlying mantle. Accordingly, the analog of the scaling law (15) is

$$\frac{U_{\text{SP}}}{V_{\text{Stokes}}} = \text{fct}\left(\text{St}, \theta_0, \frac{L_{\text{SP}}}{\ell}\right). \quad (16)$$

Both θ_0 and L_{SP}/ℓ appear in the list of arguments because both are necessary to define the geometrical similarity of the sheet's whole midsurface.

Guided by the proposed scaling law (16), we plot in fig. 6 the dimensionless SP speed $U_{\text{SP}}/V_{\text{Stokes}}$ as a function of L_{SP}/ℓ for several values of St and $\theta_0 = 30^\circ$. The flexural stiffness St was adjusted by varying both the viscosity ratio λ_1 and the slab length ℓ , which directly affects ℓ_b . Three aspects of the results are noteworthy. First, the six curves in fig. 6 are nonintersecting and appear from top to bottom in order of increasing St, which validates the assumed form (16) of the scaling law. Second, each curve on this semi-log plot is a nearly perfect straight line, indicating that the plate speed depends logarithmically on the plate length for a wide range of values of St. Third, the transition from the Stokes to the flexural limit is manifest in the decreasing slopes of the curves from top to bottom. For low values of St, an increase of L_{SP} increases the drag force on the base of the plate, and therefore strongly affects U_{SP} since it is the external viscosity η_0 that governs the plate's dynamics. On the other hand, for $\text{St} \gg 1$ U_{SP} becomes much less sensitive to L_{SP} since it is the internal viscosity η_1 (and no longer the basal drag) that controls the plate motion.

Both the slope α and the intercept β of the lines in fig. 6 obviously depend on St. Quantifying these relations, we find the more detailed scaling law

$$\frac{U_{\text{SP}}}{V_{\text{Stokes}}} = \beta(\text{St}) + \alpha(\text{St}) \log(L_{\text{SP}}/\ell) \quad (17)$$

where $\alpha(\text{St})$ and $\beta(\text{St})$ are shown in fig. 7. For $\text{St} \in [0.1, 20]$ and $L_{\text{SP}}/\ell \in [2, 10]$, the numerical solutions for $U_{\text{SP}}/V_{\text{Stokes}}$ collapse onto the universal curve (17) to within an error of $\pm 5\%$.

To conclude our analysis of the SP ONLY case, we quantify the convergence speed $V_{\text{Conv}} \equiv d\ell_s/dt$. A numerically stable value of this speed is obtained by running the code for three time steps and defining V_{Conv} as the best-fitting slope of the curve $\ell_s(t)$. The results are shown in fig. 8. The numerical solutions show that V_{Conv} , like V_{Sink} , does not depend on the plate length L_{SP} . However, we find that V_{Conv} depends on the ratio ℓ/h . The scaling law therefore has the general form

$$\frac{V_{\text{Conv}}}{V_{\text{Stokes}}} = \text{fct}\left(\text{St}, \theta_0, \frac{\ell}{h}\right). \quad (18)$$

The presence of ℓ/h in the list of arguments means that dynamical similarity depends on the geometry of the whole slab, and not just the geometry of its midsurface.

5.2 Instantaneous solutions: SP+OP

The next task is to determine how the presence of the OP influences the reference scaling laws (16) and (18) for the SP alone. In order to reduce the number of parameters involved, we shall vary only the OP geometry and the width of the lubrication layer between the two plates, leaving fixed the OP viscosity ratio $\lambda_2 = 10^4$ (quasi-rigid OP) and its buoyancy ratio $\Gamma = 0$ (neutrally buoyant OP). This choice is partly motivated by previous results showing that the viscosity and buoyancy of the OP play a crucial role in determining its stress state but only weakly influence the SP kinematics [Holt *et al.*, 2015].

We begin by examining the influence of different geometrical parameters on the dimensionless plate speed $U_{\text{SP}}/V_{\text{Stokes}}$, following the approach used to build figure 6. However, we now fix both the dip of the slab ($=30^\circ$) and its viscosity ratio ($=10^3$), which give

a nearly constant value of St for all configurations having the same slab length. While St depends somewhat on the OP thickness and the thickness of the lubrication layer between the two plates, the dependence on ℓ/h_{SP} and λ_1 is much stronger, and so it is plausible to consider St constant unless otherwise specified.

Fig. 9 shows the dimensionless plate speed U_{SP}/V_{Stokes} as a function of L_{SP}/ℓ for the SP+OP case. The two solid lines are for the SP ONLY and SP+OP reference cases whose parameters are given in table 3. The four dashed lines are for variations of the SP+OP reference case with respect to the parameter indicated.

The first noteworthy aspect of fig. 9 is that all the curves are straight lines. The dimensionless plate speed therefore depends logarithmically on L_{SP}/ℓ , just as it did for the SP ONLY case. We find that this dependence is general, independently of the geometry of the system.

Next, we focus on the two solid lines of figure 9 labeled as SP+OP REF and SP ONLY, whose parameters are given in table 3. We see that the presence of the OP decreases U_{SP} , but more strongly for a shorter SP. This means that the dimensionless SP speed depends on the ratio L_{SP}/L_{OP} of the lengths of the two plates. This is confirmed by comparing the SP+OP REF curve with the curve for a shorter overriding plate ($L_{OP}/h_{SP} = 10$). We choose the point with $L_{SP}/\ell = 5.45$ on the SP+OP REF curve (black star), and draw a horizontal line that meets the curve for $L_{OP}/h_{SP} = 10$ at the point with $L_{SP}/\ell = 3.15$ denoted by the white star. We find that the two starred points have similar values of the ratio $L_{SP}/L_{OP} \in [2.2, 2.4]$.

Turning to the dependence of U_{SP} on the other geometrical parameters, we see first that it is essentially independent of h_{OP} . Next, the normalized SP speed U_{SP}/V_{Stokes} increases when the slab length decreases from $7h_{SP}$ to $5h_{SP}$. This is surprising at first sight, since for a SP alone a shorter (hence stiffer) slab is associated with a lower value of U_{SP}/V_{Stokes} (fig. 6). The cause of this counterintuitive behavior lies in the presence of the OP, whose trenchward velocity decreases when ℓ/h_{SP} decreases (figure 10a). Since the SP and the OP are strongly coupled by the lubrication force in the gap between them, the SP necessarily moves faster (to the right in fig. 1) when the OP moves more slowly (to the left).

Finally, we see in fig. 9 that an increase in the lubrication gap thickness d_2 from $0.1h_{SP}$ to $0.2h_{SP}$ increases U_{SP} by a large factor ~ 1.6 . This occurs because increasing d_2 decreases the lubrication force at the subduction interface that is responsible for the coupling between the two plates.

In view of the discussion above, we can finally write the scaling law for the SP speed in the presence of an OP in the general form

$$U_{SP}/V_{Stokes} = \text{fct} \left(St, \theta_0, \frac{L_{SP}}{\ell}, \frac{\ell}{h_{SP}}, \frac{L_{SP}}{L_{OP}}, \frac{d_2}{h_{SP}} \right). \quad (19)$$

Obviously a scaling law with six arguments is too complicated to explore fully, and so we content ourselves with the results presented above.

Before turning to an examination of the convergence rate V_{Conv} , we mention two interesting features that have emerged from our analysis of the SP speed. The first concerns the driving mechanism for the motion of the OP. Two forces act on the OP: the tractions applied by the subduction-induced flow beneath its base, and the lubrication force in the subduction interface. The subduction-induced tractions are obviously the driving force, as confirmed by the fact that the OP speed is an increasing function of the parameter ℓ/h_{SP} that represents the importance of slab pull (fig. 10a). Because the sum of the forces is zero, the lubrication force must necessarily be a resisting force. This is confirmed by the fact that U_{OP} decreases as the subduction interface becomes narrower (fig. 10a). Figure 11 shows the subduction-induced flow for $\ell/h_{SP} = 7$ along with the velocity at the lower sur-

face of the OP. The vertical gradient of the horizontal velocity near the SP corresponds to a shear stress that drives the OP leftward.

The second feature concerns the dependence of U_{SP} on the interplate gap width for values $d_2 > 0.2h_{\text{SP}}$. Fig. 10b shows the dimensionless SP speed $U_{\text{SP}}/V_{\text{Stokes}}$ as a function of d_{2H}/h_{SP} for the reference case, where d_{2H} is the horizontal separation between the SP and the OP. The dashed line shows the value of $U_{\text{SP}}/V_{\text{Stokes}}$ for the corresponding SP ONLY case. Surprisingly, we find that the presence of the OP slows down the SP only for small separations $d_{2H}/h_{\text{SP}} \leq 0.65$. For larger separations, the presence of the OP makes the SP move faster by up to 75%. In the limit $d_{2H}/h_{\text{SP}} \rightarrow \infty$ the SP ONLY case is recovered.

We now turn to the influence of the OP on the dimensionless convergence speed $V_{\text{Conv}}/V_{\text{Stokes}}$. Numerical solutions show that V_{Conv} is controlled only by the geometries of the slab's midsurface and the lubrication gap, and is independent of L_{SP} , L_{OP} , and h_{OP} . In the presence of the OP, therefore, the generalized form of the scaling law (18) is

$$V_{\text{Conv}}/V_{\text{Stokes}} = \text{fct} \left(\text{St}, \theta_0, \frac{\ell}{h_{\text{SP}}}, \frac{d_2}{h_{\text{SP}}} \right) \quad (20)$$

Since the gap thickness d_2 controls the lubrication forces arising at the subduction interface, we expect that parameter to be a critical determinant of the convergence speed. Fig. 12 shows $V_{\text{Conv}}/V_{\text{Stokes}}$ as a function of the dimensionless horizontal SP/OP separation d_{2H}/h_{SP} for four values of the flexural stiffness and $\theta_0 = 60^\circ$. $V_{\text{Conv}}/V_{\text{Stokes}}$ increases strongly with the gap width $d_{2H}/h_{\text{SP}} \in [0.05, 0.35]$, and then reaches a plateau for $d_{2H}/h_{\text{SP}} \approx 1$ where the SP ONLY case (open squares) is recovered. Unlike the SP speed (fig. 10b), the convergence speed V_{Conv} never exceeds its SP ONLY value.

As a final remark, we note that fig. 12 confirms the crucial role played by the plate's stiffness St in controlling the kinematics of the SP, as we already saw in fig. 6 for the SP speed U_{SP} . Both V_{Conv} and U_{SP} decrease strongly as St increases, reflecting the overall slowing down of subduction associated with greater plate stiffness (fig. 5).

6 Thin-sheet analysis of OP deformation

In this section we focus on the subduction-induced deformation of the OP. As in the previous section, we consider only instantaneous solutions of the Stokes equations for the geometry shown in fig. 1. To simplify the notation, the arclength coordinate s_{OP} will be denoted by s .

To understand the deformation of a thin viscous sheet, it suffices to characterize the deformation of its midsurface. To do this, we solve equation (7) for points \mathbf{x} located on the OP midsurface to obtain the midsurface velocity $U(s)\mathbf{s} + W(s)\mathbf{z}$, where \mathbf{s} and \mathbf{z} are unit vectors parallel to and perpendicular to the midsurface, respectively. The deformation of the midsurface is then characterized by the rate of stretching Δ and the rate of change of curvature ('curling rate') K , which for a flat sheet are

$$\Delta = U', \quad K = W'', \quad (21)$$

where primes denote d/ds . The quantities Δ and K measure the rates of deformation of the midsurface by stretching (or shortening) and by bending, respectively.

Useful measures of the intensities of the stretching and bending deformations of a thin sheet are the rates of viscous dissipation of energy associated with each. Per unit area of the OP midsurface, these are

$$\phi_s = 4\eta_2 h_{\text{OP}} \Delta^2, \quad \phi_b = \frac{1}{3} \eta_2 h_{\text{OP}}^3 K^2, \quad (22)$$

where the subscripts s and b refer to stretching/shortening and bending, respectively. The relative magnitudes of $\phi_b(s)$ and $\phi_s(s)$ indicate which mode of deformation is dominant as a function of arclength. We note for future reference that

$$\phi_b = -MK, \quad M = -\frac{1}{3} \eta_2 h_{\text{OP}}^3 K, \quad (23)$$

where M is the bending moment.

In the rest of this section, all quantities referred to are dimensionless, having been nondimensionalized using h_{SP} as the length scale and $g\Delta\rho_1 h_{\text{SP}}^2/\eta_0$ as the velocity scale. Consequently, the rates of viscous dissipation of energy will scale as:

$$\hat{\phi} = \frac{\eta_0}{h_{\text{SP}}^3 (g\Delta\rho_1)^2} \phi \quad (24)$$

Our first task is to explore how the properties of the SP influence the deformation of the OP. Our numerical simulations show that the OP deformation depends neither on L_{SP} nor on L_{OP} , and so we set these arbitrarily to $L_{\text{SP}} = L_{\text{OP}} = 16h_{\text{SP}}$. We then fix the viscosity ratios of both plates ($\lambda_1 = \lambda_2 = 350$), the OP thickness ($h_{\text{OP}} = h_{\text{SP}}$) and the interplate gap width ($d_2/h_{\text{SP}} = 0.1$), which allows us to focus on the SP dip θ_0 and slab length ℓ/h_{SP} .

Fig. 13, at the top, shows $K(s)$ and $\Delta(s)$ as function of θ_0 for $\ell/h_{\text{SP}} = 7$ and $\Gamma = 0$. The steeper the subduction, the higher the magnitude of the bending moment in the OP. However, the length of the portion of the OP where the bending moment is significant (= bending length) is independent of θ_0 . The stretching rate Δ does not vary monotonically with the slab dip: its magnitude increases from $\theta_0 = 30^\circ$ to 60° , and then decreases from 60° to 90° . For $\theta_0 = 30^\circ$ there is weak backarc extension for $s > 2.7$.

The bottom part of fig. 13 shows $K(s)$ and $\Delta(s)$ as functions of ℓ/h_{SP} for $\theta_0 = 30^\circ$ and $\Gamma = 0$. The magnitude of the bending moment does not vary significantly with the slab length, but the bending portion of the OP becomes longer as the slab length increases. The magnitude of the compression $\Delta < 0$ is greater for longer slabs, while shorter

slabs cause weak extension in the OP. The shorter the slab, the longer the portion of the OP deforming in extension ($s > 1.5$ for $\ell/h_{\text{SP}} = 5$, $s > 2.7$ for $\ell/h_{\text{SP}} = 7$.)

On the left of fig. 14 is shown $\Delta(s)$ for two values of Γ , $\theta_0 = 30^\circ$, and $\ell/h_{\text{SP}} = 5$. In the previous figures, we saw that a short and shallowly dipping slab leads to relatively small bending and stretching deformations of the OP. However, the same two conditions are precisely those that lead to back-arc extension (around 300 km from the trench assuming $h_{\text{SP}} = 100$ km). The left-side of fig. 14 shows that the transition between compression and extension is further encouraged by OP buoyancy. For example, when $\Gamma = -0.25$ ($\Delta\rho_2 = -18 \text{ kg/m}^3$ assuming $\Delta\rho_1 = 70 \text{ kg/m}^3$), the stretching rate curve shifts upward and the length of the extension zone increases. By contrast, numerical solutions show that the curling rate K is unaffected.

Fig. 15 shows the rates of energy dissipation ϕ_b and ϕ_s for the configurations of the left part of fig. 14. The deformation changes from compression-dominated close to the trench to bending-dominated further away, a general pattern that we find for many choices of the dimensionless parameters of the model. Only for steep angles of subduction and (mainly) long slabs is the deformation of the OP almost exclusively compression-dominated. For the particular case of a positively buoyant OP ($\Gamma < 0$), fig. 15 shows that there is an additional extension-dominated domain in the backarc region beyond the bending zone.

To conclude this section, we examine the influence of the thickness of the OP and of the interplate gap on the OP deformation. As one would expect, varying the OP thickness within the range $h_{\text{OP}} \in [0.75, 1.25]$ changes K and Δ substantially, simply because the resistance of the OP to deformation is proportional to h_{OP} (for stretching) and h_{OP}^3 (for bending). Figures showing this will be provided by the authors upon request.

As for the effect of the subduction channel width d_2 , it is significant only very close to the trench. To show this, we extend leftward the OP midsurface (figure 1) into the triangular endpiece, which allows us to calculate K and Δ for $-1 \leq s \leq 0$. We report in the right part of fig. 14 Δ for three different values of d_2/h_{SP} for a case with $\ell/h_{\text{SP}} = 5$, $\theta_0 = 30^\circ$ and $\Gamma = 0$. The differences among the three curves are confined essentially to $-1 \leq s \leq 1$. In the near-trench (forearc) region $-1 \leq s \leq 0$, Δ increases in magnitude as d_2/h_{SP} diminishes, reflecting the increase of the lubrication pressure in the subduction interface. The influence of the lubrication force on the deformation of the OP essentially disappears beyond $s = 1$. The same holds true for the K curves (not shown to save space).

7 Geophysical application: evaluation of the interface viscosity of the central Aleutian slab

In this section we apply our BEM model to a real subduction zone in order to constrain the effective value of the strength of the subduction interface. We start by defining the dimensionless interface strength of a subduction zone as

$$\gamma = \frac{\eta_{SI}}{\eta_0} \frac{h_{SP}}{d_2} \quad (25)$$

where η_{SI} is the viscosity of the fluid in the subduction interface channel. Equation (25) arises from the definition of the shear force acting on the SP across the subduction interface, and implies that the interface strength can be increased either by increasing its viscosity or decreasing its thickness d_2 . In our model, $\eta_{SI} \equiv \eta_0$ is constant, but this does not matter because only the ratio η_{SI}/d_2 is dynamically significant. Thus we can vary the strength of the subduction interface by varying d_2 alone.

The next step is to choose a subduction zone that can be reasonably approximated by our model. Perusing the database of Lallemand *et al.* [2005], we decided to focus on the central Aleutian subduction zone. There are two main reasons for this choice. First, this portion of the Aleutian slab is far from the edges of the subduction zone, making it reasonable to use a 2-D model with no toroidal flow. This approximation is validated by the similarity of the geometries and subduction rates among the three neighboring central Aleutian transects listed in table 4. Second, the central Aleutian slab extends to depths of only 500-550 km, and so has not yet interacted with a potential viscosity jump at the 660 km discontinuity. Our model with a constant mantle viscosity is therefore reasonable for subduction in the Aleutian region. The particular value of the viscosity that we choose is discussed below.

Having selected the subduction zone, we specify the corresponding configuration of our BEM model by averaging the properties given for the three transects CALE4, CALE5 and CALE6 tabulated by Lallemand *et al.* [2005]. Table 4 gives the relevant parameters for these transects, together with a list ('BEM-segment') of the parameters adopted for the simulation. The lengths L_{SP} and L_{OP} of the two plates have been computed as the square roots of the approximate areas of the subducting Pacific plate ($\approx 10^8$ km²) and the over-riding North American plate ($\approx 8 \times 10^7$ km²). However, the choice of the two lengths is somewhat arbitrary since the target parameter of our analysis, V_{Conv} , depends neither on L_{SP} nor on L_{OP} (§ 5.2).

Having defined the geometry of the subduction zone, we then run the model for a reasonable range [Ribe, 2010] of the viscosity ratios of the two plates, $\lambda_1 = \lambda_2 \in [150-450]$, and for a range of values of the dimensionless interface strength $\gamma \in [0.5-20]$. This yields curves of the dimensionless convergence rate as a function of γ . Next, we dimensionalize the calculated convergence rates by multiplying by the velocity scale V_{Stokes} given by equation (13). To calculate V_{Stokes} , we assume $h_{SP} = 100$ km and $\Delta\rho_1 = 70$ kg m⁻³, and take η_0 to be the depth-averaged viscosity in the range 0-1000 km inferred by Mitrovica & Forte [2004]. Taking into account the error bars on the viscosities estimated by Mitrovica & Forte [2004], we find that the minimum, best-estimate, and maximum values of η_0 are

$$\eta_{0(-)} \sim 3.92 \times 10^{20} \text{ Pa s}, \quad \eta_{0(\text{Best})} \sim 5.44 \times 10^{20} \text{ Pa s}, \quad \eta_{0(+)} \sim 6.95 \times 10^{20} \text{ Pa s}. \quad (26)$$

Thus, we can now obtain the corresponding value of V_{Conv}/V_{Stokes} for the 'BEM-segment' as a function of the mantle viscosities given in (26) and find the range of γ on the curves $V_{Conv}/V_{Stokes} = \text{fct}(\gamma)$ that predicts the observed convergence rate. Figure 16 shows the final result, where we find $\gamma \in [1.97-6.25]$. To estimate the corresponding viscosity of the subduction interface, we assume $d_2/h_{SP} \sim 0.07$, which is equivalent to assuming that the subduction interface is the oceanic crust. We then find from equation (25) that $\eta_{SI} = 0.96-1.72 \times 10^{20}$ Pa s.

8 Discussion

The main goal of this study has been to get a clearer picture of the mechanics of subduction, and particularly to explore the role played by the subduction interface. Figure 17 is a schematic diagram of the overall dynamical picture that arises from our work.

Consider first the SP and its characteristic velocities V_{Conv} and U_{SP} . Figure 17 helps understand the critical role of the subduction interface thickness ratio d_2/h_{SP} that appears in the scaling laws (20) for V_{Conv} and (19) for U_{SP} . Once the slab's geometrical parameters (θ_0 and ℓ/h_{SP}) are fixed and a certain value of the flexural stiffness ($St \equiv F_{\text{int}}/F_{\text{D(Slab)-}}$) is obtained, the remaining forces affecting the SP are the drag force $F_{\text{D(SP)-}}$ on its trailing (non-bending) portion and the lubrication forces F_t and F_n on the interface. However, we saw in § 5.2 that the length of the trailing part of the SP, and therefore also the drag force $F_{\text{D(SP)-}}$, has no influence on V_{Conv} . Accordingly, it is mainly the shear force F_t that opposes the convergence. Since $F_t \propto \eta_{\text{SI}}/d_2$, V_{Conv} is smaller for a thinner (stronger) lubrication gap and larger for a thicker (weaker) one. Turning now to U_{SP} we recall that this velocity, unlike V_{Conv} , does depend on the trailing plate length and hence also on $F_{\text{D(SP)-}}$. More precisely, U_{SP} is influenced by the sum of $F_{\text{D(SP)-}}$ and the horizontal resultant of the lubrication forces F_t and F_n . Thus, again, lower values of d_2 will generally decrease U_{SP} , while higher ones will increase it.

In the derivation of the scaling law (19) for U_{SP} , two other interesting features have emerged. The first is that U_{SP} , unlike V_{Conv} , depends also on the horizontal speed of the OP as explained in § 5.2. It follows that two different geometrical configurations will have the same value of U_{SP} only if the value of U_{OP} does not change, i.e., if $U_{\text{SP}}/U_{\text{OP}}$ is constant. This explains why the ratio $L_{\text{SP}}/L_{\text{OP}}$ appears in the scaling law (19). Among the forces acting on the OP, the only one that depends on L_{OP} is the resisting drag $F_{\text{D(OP)-}}$, since the driving shear force $F_{\text{D(OP)+}}$ is determined by the mantle return flow within the wedge and is always confined to the forearc region of the OP. Thus when we vary L_{SP} or L_{OP} with all other geometrical parameters held constant, only the two drag forces that oppose the motion of the two horizontal plates change. Accordingly, configurations with the same ratio $L_{\text{SP}}/L_{\text{OP}}$ will also have the same ratio $F_{\text{D(SP)-}}/F_{\text{D(OP)-}}$ and, consequently, a constant speed ratio $U_{\text{SP}}/U_{\text{OP}}$. This is confirmed by table 5 for the configurations with different values of $L_{\text{SP}}/L_{\text{OP}}$ that were shown in § 5.2, fig. 9.

The second noteworthy aspect of the scaling law (19) is the near-perfect logarithmic dependence of U_{SP} on the ratio L_{SP}/ℓ . Although U_{SP} is still correlated with the negative buoyancy ($F_b \propto \ell$) that drives the plate and with the resisting drag force measured by the plate length L_{SP} , the dependence between these two quantities turns out to be surprisingly weak, namely logarithmic. This feature seems to agree with observations in nature, where the speeds of plates attached to subducting slabs are poorly correlated with their lengths [Conrad & Hager, 1999].

Turning now to the OP, our first result concerns the forces that drive its motion. Some studies [e.g. Chen *et al.*, 2015] conclude that the interplate lubrication force, depending on the configuration of the system, may drive, rather than resist, the motion of the OP. However, we find that the opposite is always the case. As shown in fig. 2c (inset), the subduction interface evolves so that it is narrower at the bottom than at the top. The downgoing plate therefore drags fluid from the wider to the narrower part of the gap. According to lubrication theory, this is just the condition for the existence of a positive pressure within the gap, which is what keeps the two plates apart. Accordingly, the normal force in the gap resists, rather than drives, the leftward motion of the OP, regardless of the geometry of the plates or the initial gap thickness. The role of the gap thickness is underlined by fig. 10a, which shows that U_{OP} decreases as the lubrication force increases with decreasing d_2 . Now, since $F_{\text{D(OP)-}}$ represents an additional resisting force associated with the mantle flow below most of the OP, we conclude that the sole driving force is the shear force $F_{\text{D(OP)+}}$. This force is related to the vertical gradient of horizontal velocity

beneath the forearc region of the OP (visible in fig. 11). This means that the only way to increase U_{OP} is to increase the slab length ℓ , which leads to a more vigorous return flow below the OP and a larger $F_{D(OP)+}$.

A second result concerns the mechanism of deformation of the OP. According to thin viscous-sheet theory, the deformation of a thin sheet occurs by a combination of stretching/shortening and bending. The relative importance of these two deformation modes is measured by the rates of viscous dissipation of energy (ϕ_s and ϕ_b , respectively) associated with them. Calculating these as a function of arclength along the midsurface of the OP, we found the general pattern shown in fig. 15. Within a distance $1-1.5h_{SP}$ from the trench ($s = 0-0.5h_{SP}$) the deformation is always dominated by compression. This is due to the opposing actions of the (rightward) horizontal resultant of the interplate lubrication force and the (leftward) driving shear force below the forearc region. Further from the trench, bending usually becomes dominant (fig. 18). The exception is for larger values of the slab length ℓ and the initial dip θ_0 , for which compression may dominate over bending everywhere. This is seen in table 6, where the case $\ell/h_{SP}=7$ and $\theta_0= 60^\circ$ has no region dominated by bending.

Still further from the trench, in the back-arc region of the OP, both compression and bending are negligible if the OP is neutrally buoyant ($\Gamma = 0$). However, when the OP is positively buoyant ($\Gamma < 0$), significant stretching of the back-arc region occurs (fig. 14, on the left). In particular, a simple lubrication-theory model for an isolated OP (Appendix A:) shows that the dimensionless stretching rate Δ of the back-arc region is

$$\Delta = -\frac{d_1\Gamma}{4\lambda_2}, \quad (27)$$

which is positive (extensional) if $\Gamma < 0$. This result is only indicative because the model of an isolated OP treated in Appendix A: ignores the substantial shear traction generated below the forearc region of the OP by the slab-induced mantle flow. Nevertheless, eq. (27) is consistent with the fact that back-arc extension only occurs in numerical solutions when $\Gamma < 0$. A similar result has been reported by Holt *et al.* [2015] for a model in which the upper surface of the OP is itself a free-slip surface. We show in Appendix B: that the horizontal extensional stress found numerically by Holt *et al.* [2015] agrees almost exactly with the prediction of a simple plug-flow model for a spreading viscous gravity current.

The last result regarding the OP deformation concerns the influence of the subduction interface. Our model confirms the short-range nature of the lubrication forces that develop within the subduction interface, as also reported by Duarte *et al.* [2013] and Chen *et al.* [2015]. In fact, as reported at the end of § 6 varying the thickness of the lubrication layer (i.e. the magnitude of the lubrication forces) influences both the shortening (right of fig. 14) and the bending of the OP, but only in the forearc region.

In conclusion, we compare the range of values of the dimensionless interface strength γ constrained by our work with values assumed in or constrained by other published subduction models. As shown in table 7, these values vary by a factor $90/0.13 \sim 700$, with our inferences (2.0-6.3) being squarely in the middle of the range. Two important aspects of the numbers in table 7 require some comments.

First, we note that three studies (denoted by asterisks) infer values of γ from natural data. Of these, the study of Duarte *et al.* [2015] stands out on account of its very large estimate $\gamma \approx 90$. However, in this study there is a large uncertainty concerning the characterization of the interface between the two plates. The laboratory experiment starts with the two plates separated by a horizontal distance $d_{2H} \sim 1$ cm that is comparable to the thickness $h_{SP} \sim 1.6$ cm of the SP. As subduction proceeds, the two plates move closer together, until they are separated by a thin (≈ 1 mm) interface when the SP approaches the bottom of the tank. The ratio d_2/h_{SP} thus varies within a range $[0.06, 0.63]$ in the course of the experiment. The value $\gamma \approx 90$ in table 7 is calculated for the smallest value of $d_2/h_{SP} = 0.06$.

Second, when plate velocities observed in nature are used to infer γ the assumed value of the viscosity ratio λ_1 between the SP and the mantle is critical [Duarte *et al.*, 2015]. This is clear in fig. 16, where the point of intersection between the horizontal lines (= real velocity of the transect) and the curves for different λ_1 varies significantly. This can be explained using the scaling law (20) for the convergence speed of the SP. Once the slab's geometry is fixed, V_{Conv} depends on the flexural stiffness St and the ratio d_2/h_{SP} (or γ if we also take into account the viscosity ratio η_{SI}/η_0). Now since the geometry is fixed, eq. (14) shows that St depends only on λ_1 , because the bending length ℓ_b itself does [Ribe, 2010]. We can therefore write

$$V_{\text{Conv}} = \text{fct}(\lambda_1, \gamma) \quad (28)$$

for a model configuration where the geometry is known. Thus, if we fix V_{Conv} to a value obtained from natural data, the value of λ_1 will be crucial in determining the corresponding value of γ . In physical terms, lower values of λ_1 speed up the SP so that a stronger interface (higher γ) is needed for a given V_{Conv} , and vice versa. Accordingly, a better constraint on the interface strength of real subduction zones requires a more precise knowledge of the viscosity ratio between the SP and the underlying mantle.

9 Conclusions

In this work we studied the dynamics of subduction by means of a numerical model based on the boundary-element method (BEM). Systematically interpreting the results in the light of thin-viscous sheet theory, we explored the kinematics of the SP and the deformation of the OP, particularly focusing on the influence of the subduction interface on those aspects.

Regarding the kinematics of the SP, we first found a scaling law that describes the convergence speed of the descending slab. Neither the length of the SP nor that of the OP influences the convergence rate, which is instead controlled by the slab's shape, the flexural stiffness St of the plate, and the strength of the subduction interface. The convergence rate increases as either the stiffness of the plate or the strength of the subduction interface decreases. Next, we considered the horizontal speed U_{SP} of the flat portion of the plate. For the case of an isolated SP, U_{SP} obeys the scaling law $U_{SP}/V_{Stokes} = \alpha(St) + \beta(St) \log(L_{SP}/\ell)$, where α and β are logarithmic functions of St . Adding the OP to the system, the scaling law becomes rather complex, with both the strength of the interface and the length of the OP now being dynamically relevant. However, numerical solutions still show a perfect logarithmic dependence of U_{SP}/V_{Stokes} on L_{SP}/ℓ . This very weak correlation between plate speed and plate length for plates attached to subducting slabs seems to be in agreement with natural observations.

Turning to the OP, we found a three-zone pattern of deformation that is similar for the majority of cases we explored. Close to the trench, the OP is always under strong compression due to the opposing actions of the horizontal resultant of the lubrication force within the subduction interface and the shear force below the forearc region of the OP. The latter force derives from the mantle return flow and is the sole force driving OP motion. Further from the trench is a second zone of deformation dominated by bending, except for long subducting slabs and steep subduction angles for which compression continues to dominate. Finally, significant extension appears in the back-arc region when the OP is positively buoyant, a result that we explained using simple analytical thin-layer models.

We concluded by using the BEM model to constrain the interface viscosity η_{SI} of a natural subduction zone, the central portion of the Aleutian subduction zone. For a realistic range of values of the viscosity ratio between the SP and the underlying mantle, we found $\eta_{SI} = 0.96 - 1.72 \times 10^{20}$ Pa s for a corresponding range of mantle viscosities $\eta_0 = 3.92 - 6.95 \times 10^{20}$ Pa s.

A: Stretching rate of a thin-viscous sheet below a lubrication layer bounded by a free-slip surface

Our goal is to show that a positively buoyant OP beneath a thin lubrication layer tends to deform in extension. For this purpose, we consider an isolated OP, and assume that the shear stress acting on its upper surface is much larger than that on its lower surface. To simplify the notation, we set $x_1 \rightarrow s$, $x_2 \rightarrow z$, and $u_1 \rightarrow u$. The global force balance in the horizontal (s -) direction is [Ribe, 2001]

$$(4\eta_2 h_{OP} U')' + \sigma_{sz}|_{z=-d_1} = 0 \quad (\text{A.1})$$

where primes denote d/ds , $\sigma_{sz}|_{x_2=-d_1}$ is the shear stress acting on the upper surface of the OP, and the quantity in parentheses is the integral of the fibre stress $\sigma_{s,s}$ across the OP. To determine σ_{sz} in the lubrication layer, we start from the s -component of the momentum equation in the lubrication limit, which is

$$p' = \eta_0 \frac{\partial^2 u}{\partial z^2} \quad (\text{A.2})$$

Since the OP is much more viscous than the lubrication layer, the effective boundary condition on the horizontal velocity is $u|_{z=-d_1} = 0$. Integrating eq. (A.2) subject to that condi-

tion and the free-slip surface condition $\partial u/\partial z|_{z=0} = 0$, we obtain

$$\sigma_{sz}(s, -d_1) \approx \eta_0 \frac{\partial u}{\partial z}(s, -d_1) = -p' \frac{d_1}{\eta_0}. \quad (\text{A.3})$$

Eq. (A.1) then becomes

$$4\eta_2 h_{\text{OP}} U'' - p' d_1 = 0 \quad (\text{A.4})$$

Now integrate eq. (A.4) once subject to the condition that both U' and p vanish at $s = 0$, which yields

$$U' = \frac{d_1}{4\eta_2 h_{\text{OP}}} p. \quad (\text{A.5})$$

Now the pressure in the OP is given by the solution of Ribe [2010], viz.,

$$\frac{p}{h_{\text{OP}} g \Delta \rho_2} = -1 + \exp(-s/\ell_0) - \frac{2}{\sqrt{3}} \exp(-s/2\ell_0) \sin \frac{\sqrt{3}s}{2\ell_0}, \quad (\text{A.6})$$

where

$$\ell_0 = \left(\frac{\lambda_2 h_{\text{OP}}^3 d_1^3}{9} \right)^{1/6}. \quad (\text{A.7})$$

Combining (A.5) and (A.6), we obtain

$$\frac{4\eta_2}{d_1 g \Delta \rho_2} U' = -1 + \exp(-s/\ell_0) - \frac{2}{\sqrt{3}} \exp(-s/2\ell_0) \sin \frac{\sqrt{3}s}{2\ell_0}. \quad (\text{A.8})$$

Eq. (A.8) describes the stretching rate of an OP that is sufficiently long that the two ends do not influence each other. Far from the ends of the OP ($s \gg \ell_0$), the stretching rate is

$$U' = -\frac{d_1 g \Delta \rho_2}{4\eta_2}, \quad (\text{A.9})$$

which shows that the OP deforms by extension ($U' > 0$) if it is positively buoyant ($\Delta \rho_2 < 0$).

We now verify our assumption that the shear stress on the lower surface of the OP ($= F_s^-$) is negligible compared to that on the upper surface ($= F_s^+$). Consider the portion of the OP of length $\sim \ell_0$ adjoining the end $s = 0$, where the shear stress on the bottom surface is largest. From the above solution, we already know that

$$F_s^+ \sim p' d_1 \sim h_{\text{OP}} g \Delta \rho_2 / \ell_0, \quad (\text{A.10})$$

where the scale for p' comes from eq. (A.6). Now, the shear stress on the base of the OP is

$$F_s^- \sim \eta_2 W / \ell_0 \sim d_1^{3/2} g \Delta \rho_2 / \sqrt{\lambda_2 h_{\text{OP}}}, \quad (\text{A.11})$$

where the scale for W comes from eq. (B6) of Ribe [2010]. Taking the ratio of the two stresses and using eq. (A.7), we obtain

$$\frac{F_s^-}{F_s^+} \sim \lambda_2^{-1/3} \left(\frac{d_1}{h_{\text{OP}}} \right). \quad (\text{A.12})$$

For small values of d_1/h_{OP} and large viscosity contrasts λ_2 (as in our study), $F_s^-/F_s^+ \ll 1$.

The analysis above is for an isolated OP, and succeeds in showing that a positively buoyant OP should deform in extension. However, in our BEM model the OP is not isolated, but is strongly influenced by the shear stress induced on its base by the sinking of the neighboring slab. This additional shear stress is much larger than F_s^+ , and so our assumption $F_s^- \ll F_s^+$ breaks down. The results of the derivation above should therefore be interpreted as indicative rather than as an accurate reflection of the BEM model.

B: Spreading gravity current below a free-slip surface

Inspired by the model of Holt *et al.* [2015], we consider a buoyant layer of fluid (the OP) bounded above by a free-slip surface. The OP has thickness h_{OP} , density ρ_{OP} and viscosity η_{OP} , while the underlying fluid has density $\rho_{\text{M}} = \rho_{\text{OP}} - \Delta\rho$ and viscosity $\eta_{\text{M}} \ll \eta_{\text{OP}}$. To lowest order, the horizontal velocity is constant across the layer (plug flow). The horizontal force balance within the layer is [Canright & Morris, 1993]

$$\frac{\partial}{\partial s} \left[h_{\text{OP}}^2 + 8h_{\text{OP}} \left(\frac{\eta_{\text{OP}}}{g\Delta\rho} \right) U' \right] = 0 \quad (\text{B.1})$$

where $U' = \partial U / \partial s$. Integrating (B.1) once, we obtain

$$h_{\text{OP}}^2 + 8h_{\text{OP}} \left(\frac{\eta_{\text{OP}}}{g\Delta\rho} \right) U' = F, \quad (\text{B.2})$$

where F is a constant. At the ends of the OP, $U' = h_{\text{OP}} = 0$, which requires $F = 0$. Therefore

$$U' = -\frac{h_{\text{OP}}g\Delta\rho}{8\eta_{\text{OP}}}. \quad (\text{B.3})$$

Now from thin viscous-sheet theory, the horizontal normal stress in the OP is $\sigma_{ss} = 4\eta_{\text{OP}}U'$, or

$$\sigma_{ss} = -\frac{h_{\text{OP}}g\Delta\rho}{2}. \quad (\text{B.4})$$

With the values $h_{\text{OP}} = 80$ km and $\Delta\rho = -130$ kg m⁻³ used by Holt *et al.* [2015], eq. (B.4) gives $\sigma_{ss} \approx 50$ MPa. This agrees almost exactly with the numerical prediction of fig. 15a of Holt *et al.* [2015].

C: Numerical implementation

We ran all the simulations using a non-uniform mesh with increased resolution along the upper surfaces of the plates and along the portions adjoining the subduction interface (figure 19). This choice follows from the requirement that the distance between the observation point and the integration point in the Green’s functions used in the BEM approach must always be larger than the size of the element in order to avoid loss of accuracy [Pozrikidis, 1992]. In our problem, this requires paying particular attention to the discretization of the subduction interface where two surfaces are close together.

With these considerations in mind, we built our mesh as follows. We began by choosing the lower limit of the interface thickness upon which to calibrate the corresponding resolution at the interface. Once this is done, we can safely go to wider interfaces being sure that the accuracy criterion explained above is satisfied. We fixed this value at $d_2 = 0.08h_{SP}$, which represents a robust limit to simulate sufficiently strong interfaces ($\gamma = 12.5$) in a wide range of viscosity ratios, i.e. $10^2 \leq \lambda_i \leq \times 10^5$, $i = 1$ or 2 . Thinner interfaces (e.g., $d_2 = 0.05h_{SP}$) could have been adopted but not in combination with high viscosity ratios ($\lambda_i > 5 \times 10^4$) for which we obtained unphysical flow fields. Next, we imposed a reasonable resolution for the lower surface of the plates ($=0.1h_{SP}$) and we quadrupled it at the interface obtaining a constant element size of $\approx 0.025h_{SP}$. For the instantaneous solutions of the model, this mesh represents a good balance between accuracy and computational cost: decreasing the resolution by a factor of 2 led to an average error of 10% while increasing it by the same factor resulted in exactly the same flow field but with a significant slowdown in the computational time.

Finally, we made sure that the mesh maintained adequate resolution during time-dependent simulations. In principle, the natural evolution of the interface (not constrained with any ‘contact algorithm’) could reduce the thickness of the lubrication layer to below the fixed element size $0.025h_{SP}$. To verify that this does not occur, we started from an initial SI thickness $d_2 = 0.08h_{SP}$ and let the system evolve until the slab’s tip reached the depth $x_2 = -6.6h_{SP}$, keeping track of the minimum distance $d_2^{min}(t)$ between the two plates. We observed that d_2^{min} never went below ≈ 0.068 , so that the accuracy criterion was fulfilled. We also verified that doubling the resolution of the mesh did not result in any significant changes in the computed flow field.

Acknowledgments

This work has received funding from the European Union’s Horizon 2020 research and innovation programme under the Marie-Sklodowska-Curie grant agreement No 642029-ITN CREEP. It was supported by the Programme National de Planétologie (PNP) of CNRS/INSU, co-funded by CNES. The authors thank all the CREEP network for inspiring and helpful discussions. A. Davaille, L. Fleitout and B. Kaus are particularly thanked for their constructive suggestions. Careful reviews by J. Duarte and G. Morra helped greatly to improve the manuscript. All data and methods necessary to understand, evaluate and replicate the reported research are presented in the manuscript.

References

- Babeyko, A. & Sobolev, S. High-resolution numerical modeling of stress distribution in visco-elasto-plastic subducting slabs. *Lithos*, 103(1):205–216, 2008.
- Bellahsen, N., Faccenna, C., & Funiciello, F. Dynamics of subduction and plate motion in laboratory experiments: insights into the “plate tectonics” behavior of the earth. *Journal of Geophysical Research: Solid Earth*, 110(B1), 2005.
- Bottrill, A. D., van Hunen, J., & Allen, M. B. Insight into collision zone dynamics from topography: numerical modelling results and observations. *Solid Earth*, 3(2):387, 2012.
- Butterworth, N., Quevedo, L., Morra, G., & Müller, R. Influence of overriding plate geometry and rheology on subduction. *Geochemistry, Geophysics, Geosystems*, 13(6), 2012.
- Canright, D. & Morris, S. Buoyant instability of a viscous film over a passive fluid. *Journal of Fluid Mechanics*, 255:349–372, 1993.
- Chen, Z., Schellart, W. P., & Duarte, J. C. Overriding plate deformation and variability of fore-arc deformation during subduction: Insight from geodynamic models and application to the calabria subduction zone. *Geochemistry, Geophysics, Geosystems*, 16(10): 3697–3715, 2015.
- Chen, Z., Schellart, W. P., Strak, V., & Duarte, J. C. Does subduction-induced mantle flow drive backarc extension? *Earth and Planetary Science Letters*, 441:200–210, 2016.
- Conrad, C. P. & Hager, B. H. Effects of plate bending and fault strength at subduction zones on plate dynamics. *Journal of Geophysical Research: Solid Earth*, 104(B8): 17551–17571, 1999.
- Di Giuseppe, E., Van Hunen, J., Funiciello, F., Faccenna, C., & Giardini, D. Slab stiffness control of trench motion: Insights from numerical models. *Geochemistry, Geophysics, Geosystems*, 9(2), 2008.
- Duarte, J. C., Schellart, W. P., & Cruden, A. R. Three-dimensional dynamic laboratory models of subduction with an overriding plate and variable interplate rheology. *Geophysical Journal International*, 195(1):47–66, 2013.
- Duarte, J. C., Schellart, W. P., & Cruden, A. R. How weak is the subduction zone interface? *Geophysical Research Letters*, 42(8):2664–2673, 2015.
- Funiciello, F., Moroni, M., Piromallo, C., Faccenna, C., Cenedese, A., & Bui, H. A. Mapping mantle flow during retreating subduction: Laboratory models analyzed by feature tracking. *Journal of Geophysical Research: Solid Earth*, 111(B3), 2006.
- Funiciello, F., Faccenna, C., Heuret, A., Lallemand, S., Di Giuseppe, E., & Becker, T. Trench migration, net rotation and slab–mantle coupling. *Earth and Planetary Science Letters*, 271(1):233–240, 2008.
- Garel, F., Goes, S., Davies, D., Davies, J. H., Kramer, S. C., & Wilson, C. R. Interaction of subducted slabs with the mantle transition-zone: A regime diagram from 2-d thermo-mechanical models with a mobile trench and an overriding plate. *Geochemistry, Geophysics, Geosystems*, 15(5):1739–1765, 2014.
- He, L. Influence of lithosphere-asthenosphere interaction on the overriding lithosphere in a subduction zone: Numerical modeling. *Geochemistry, Geophysics, Geosystems*, 13(2), 2012.

- Holt, A., Becker, T., & Buffett, B. Trench migration and overriding plate stress in dynamic subduction models. *Geophysical Journal International*, 201(1):172–192, 2015.
- Kincaid, C. & Olson, P. An experimental study of subduction and slab migration. *Journal of Geophysical Research: Solid Earth*, 92(B13):13832–13840, 1987.
- Klein, E., Fleitout, L., Vigny, C., & Garaud, J. Afterslip and viscoelastic relaxation model inferred from the large-scale post-seismic deformation following the 2010 m w 8.8 maule earthquake (Chile). *Geophysical Journal International*, 205(3):1455–1472, 2016.
- Krien, Y. & Fleitout, L. Gravity above subduction zones and forces controlling plate motions. *Journal of Geophysical Research: Solid Earth*, 113(B9), 2008.
- Lallemand, S., Heuret, A., & Boutelier, D. On the relationships between slab dip, back-arc stress, upper plate absolute motion, and crustal nature in subduction zones. *Geochemistry, Geophysics, Geosystems*, 6(9), 2005.
- Li, Z.-H. & Ribe, N. M. Dynamics of free subduction from 3-d boundary element modeling. *Journal of Geophysical Research: Solid Earth*, 117(B6), 2012.
- Manga, M. & Stone, H. Buoyancy-driven interactions between two deformable viscous drops. *Journal of Fluid Mechanics*, 256:647–683, 1993.
- Meyer, C. & Schellart, W. Three-dimensional dynamic models of subducting plate-overriding plate-upper mantle interaction. *Journal of Geophysical Research: Solid Earth*, 118(2):775–790, 2013.
- Mitrovica, J. & Forte, A. A new inference of mantle viscosity based upon joint inversion of convection and glacial isostatic adjustment data. *Earth and Planetary Science Letters*, 225(1):177–189, 2004.
- Pozrikidis, C. *Boundary integral and singularity methods for linearized viscous flow*. Cambridge University Press, 1992.
- Press, W. H., Teukolsky, S., Vetterling, W., & Flannery, B. Numerical recipes in fortran 77: the art of scientific computing, cambridge university press. *Cambridge, England* 933pp, 1992.
- Ribe, N. Bending and stretching of thin viscous sheets. *Journal of Fluid Mechanics*, 433: 135–160, 2001.
- Ribe, N. M. Bending mechanics and mode selection in free subduction: A thin-sheet analysis. *Geophysical Journal International*, 180(2):559–576, 2010.
- Rodríguez-González, J., Negrodo, A. M., & Billen, M. I. The role of the overriding plate thermal state on slab dip variability and on the occurrence of flat subduction. *Geochemistry, Geophysics, Geosystems*, 13(1), 2012.
- Schellart, W. Kinematics of subduction and subduction-induced flow in the upper mantle. *Journal of Geophysical Research: Solid Earth*, 109(B7), 2004.
- Schellart, W. Kinematics and flow patterns in deep mantle and upper mantle subduction models: Influence of the mantle depth and slab to mantle viscosity ratio. *Geochemistry, Geophysics, Geosystems*, 9(3), 2008a.
- Schellart, W. Subduction zone trench migration: Slab driven or overriding-plate-driven? *Physics of the Earth and Planetary Interiors*, 170(1):73–88, 2008b.
- Schellart, W. Evolution of subduction zone curvature and its dependence on the trench velocity and the slab to upper mantle viscosity ratio. *Journal of Geophysical Research: Solid Earth*, 115(B11), 2010.
- Schellart, W. & Moresi, L. A new driving mechanism for backarc extension and backarc shortening through slab sinking induced toroidal and poloidal mantle flow: Results from dynamic subduction models with an overriding plate. *Journal of Geophysical Research: Solid Earth*, 118(6):3221–3248, 2013.
- Schellart, W. P. & Strak, V. A review of analogue modelling of geodynamic processes: Approaches, scaling, materials and quantification, with an application to subduction experiments. *Journal of Geodynamics*, 2016.
- Shemenda, A. I. Subduction of the lithosphere and back arc dynamics: Insights from physical modeling. *Journal of Geophysical Research: Solid Earth*, 98(B9):16167–16185, 1993.

- Turcotte, D. L. & Schubert, G. *Geodynamics*, Cambridge University Press. New York, 2002.
- van Dinther, Y., Morra, G., Funiciello, F., & Faccenna, C. Role of the overriding plate in the subduction process: Insights from numerical models. *Tectonophysics*, 484(1):74–86, 2010.
- van Hunen, J., van den Berg, A. P., & Vlaar, N. J. A thermo-mechanical model of horizontal subduction below an overriding plate. *Earth and Planetary Science Letters*, 182(2):157–169, 2000.
- Wakiya, S. Application of bipolar coordinates to the two-dimensional creeping motion of a liquid. ii. some problems for two circular cylinders in viscous fluid. *Journal of the Physical Society of Japan*, 39(6):1603–1607, 1975.

Table 1. Notation

Variable	Definition	Units
d_1	Lubrication layer thickness above the plates	[m]
d_2	Lubrication layer thickness between the plates	[m]
h_{SP}	SP thickness	[m]
h_{OP}	OP thickness	[m]
L_{SP}	SP length	[m]
L_{OP}	OP length	[m]
ℓ	Slab length	[m]
θ_0	Initial dip of the slab's tip	[-]
s	Arclength coordinate along SP midsurface	[m]
s_{OP}	Arclength coordinate along OP midsurface	[m]
C_1	SP contour	[m]
C_2	OP contour	[m]
S_1	SP area	[m ²]
S_2	OP area	[m ²]
η_0	Ambient fluid viscosity	[Pa s]
ρ_0	Ambient fluid density	[kg m ⁻³]
ρ_1	SP density	[kg m ⁻³]
η_1	SP viscosity	[Pa s]
λ_1	$\equiv \eta_1/\eta_0$; SP viscosity contrast	[-]
ρ_2	OP density	[kg m ⁻³]
η_2	OP viscosity	[Pa s]
λ_2	$\equiv \eta_2/\eta_0$; OP viscosity contrast	[-]
ℓ_b	Bending length	[m]

Table 2. Initial configurations

	SP				OP				
	θ_0	L_{SP}/h_{SP}	ℓ/h_{SP}	λ_1	d_2/h_{SP}	L_{OP}/h_{SP}	h_{OP}/h_{SP}	λ_2	Γ
figure 2a	30°	16	5	300	-	-	-	-	-
figure 2b	30°	16	5	300	0.2	16	1	300	-0.25
figure 2c	30°	16	5	300	0.08	16	1	300	-0.25

Table 3. Configuration of the reference cases

	SP			OP		
	θ_0	ℓ/h_{SP}	λ_1	d_2/h_{SP}	L_{OP}/h_{SP}	h_{OP}/h_{SP}
SP ONLY	30°	7	10 ³	-	-	-
SP+OP REF	30°	7	10 ³	0.1	16	1

Table 4. Geometry and convergence rates of the 3 transects of the central Aleutian slab derived from Lallemand *et al.* [2005]. We assume $h_{SP} \sim 100$ km. The last line (‘BEM-segment’) describes the configuration adopted for the simulation and it reports the corresponding value of V_{Conv} adopted for the comparison.

Observed parameters							
	V_{Conv} [mm yr ⁻¹]	θ_0	ℓ [km]	Depth [km]			
CALE4	61.00	58.00°	704	550			
CALE5	61.00	59.00°	708	550			
CALE6	59.00	62.00°	640	500			
Simulation parameters							
	V_{Conv} [mm yr ⁻¹]	θ_0	ℓ/h_{SP}	L_{SP}/h_{SP}	L_{OP}/h_{SP}	h_{OP}/h_{SP}	Γ
‘BEM-segment’	60.33	59.67°	6.84	100.00	70.00	1.25	-0.25

Table 5. Horizontal speed ratio of the configurations shown in § 5.2 fig. 9

Points	L_{SP}/L_{OP}	U_{SP}/U_{OP}
★, ☆	2	0.49
■, □	4	0.38

Table 6. Length of the portion of the OP midsurface where the deformation is bending-dominated. We report 4 different $\ell/h_{\text{SP}}, \theta_0$ pairs. The other parameters of the model are the ones corresponding to the cases shown in fig. 13.

ℓ/h_{SP}	θ_0	Width
5	30°	$s \in [0.5 - 2.5]$
5	60°	$s \in [0.8 - 2.5]$
7	30°	$s \in [1.5 - 3.0]$
7	60°	none

Table 7. Dimensionless interface strength of different subduction models. Asterisks indicate studies where γ has been inferred by comparison with geophysical observations.

Study	Type	γ	λ_1	Rheology
This study*	Numerical	2.0-6.3	150-450	Linear
Meyer & Schellart [2013]	Experimental	0.13-0.43	200	Linear
Duarte <i>et al.</i> [2015]*	Experimental	≤ 90	160	Linear (visco-plastic interface)
Chen <i>et al.</i> [2015]	Experimental	5.3-10.00	200	Linear (visco-plastic interface)
Holt <i>et al.</i> [2015]	Numerical	0.73-1.80	100-2000	Visco-plastic
Klein <i>et al.</i> [2016]*	Numerical	0.17-1.3	Elastic lithosphere	Visco-elastic asthenosphere
	(inversion from GPS data)			

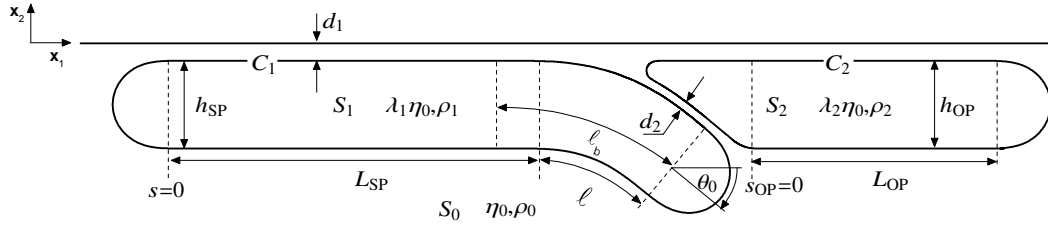


Figure 1. 2D model geometry of free subduction of a dense subducting plate (SP) with viscosity $\eta_1 = \lambda_1 \eta_0$ and density ρ_1 beneath an overriding plate (OP) with viscosity $\eta_2 = \lambda_2 \eta_0$ and density ρ_2 in an ambient fluid with viscosity η_0 and density ρ_0 . The ambient fluid is infinitely deep and is bounded at $x_2=0$ by a free-slip surface. The arclength coordinate along the SP's midsurface is $s \in [0, L_{SP} + \ell]$, while it is $s_{OP} \in [0, L_{OP}]$ for the OP arclength coordinate. The symbol ℓ_b identifies the 'bending length' of the SP, equal to the sum of the slab length and the length of the seaward portion of the SP where flexural bulging occurs (see section 5.1 for more details).

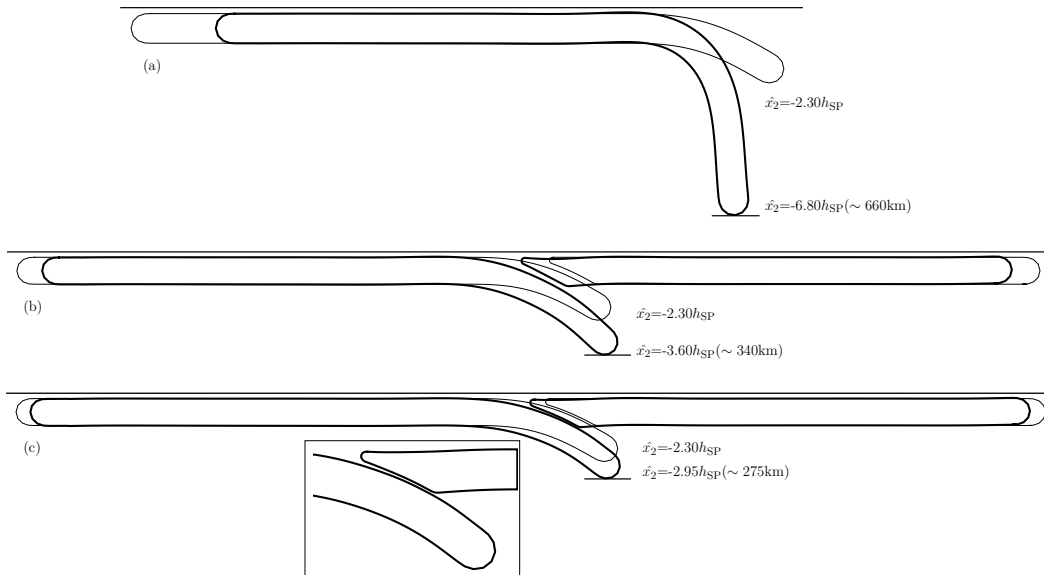


Figure 2. Time evolution of free subduction for different configurations: (a) SP ONLY case, (b) SP+OP case with $d_2/h_{SP}=0.2$, (c) SP+OP case with $d_2/h_{SP}=0.08$. In all cases the thin solid line represents the initial configuration of the system specified in table 2, while the thick solid line corresponds to the final state of the sheets at the dimensionless time $\hat{t} = t h_{SP} g \Delta \rho_1 / \eta_0 = 21.5$. The vertical coordinate \hat{x}_2 of the deepest point on the slab and its equivalent in km are indicated. The inset of (c) is a zoomed-in view of the final state of the system.

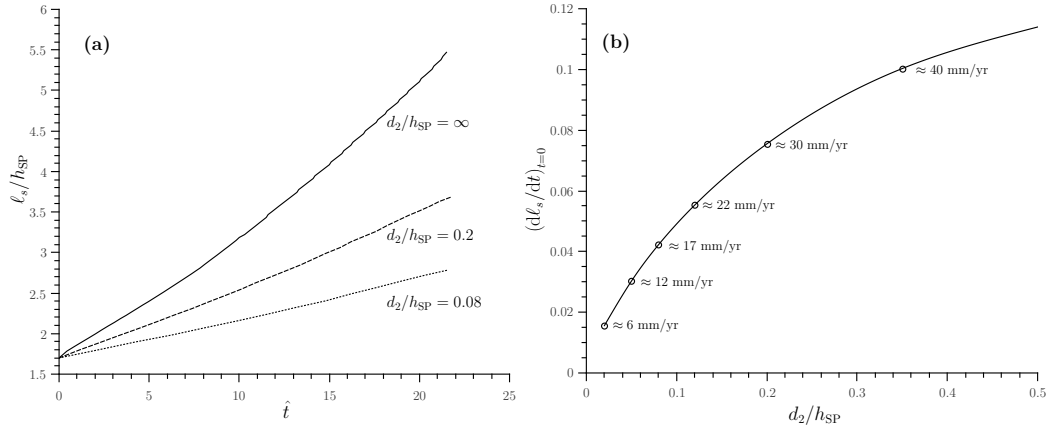


Figure 3. Dependence of the convergence rate on the thickness of the subduction interface. (a) Subducted length ℓ_s of the midsurface of the SP as a function of time for the three cases of fig. 2. The values of d_2/h_{SP} indicated are initial values ($t = 0$). (b) Instantaneous convergence rate of the initial configuration as a function of the dimensionless gap width d_2/h_{SP} . The dimensional convergence rates indicated are calculated from eq. (6) assuming $h_{SP} = 100$ km, $\eta_0 = 5.44 \times 10^{20}$ Pa s, and $\Delta\rho_1 = 70$ kg m $^{-3}$.

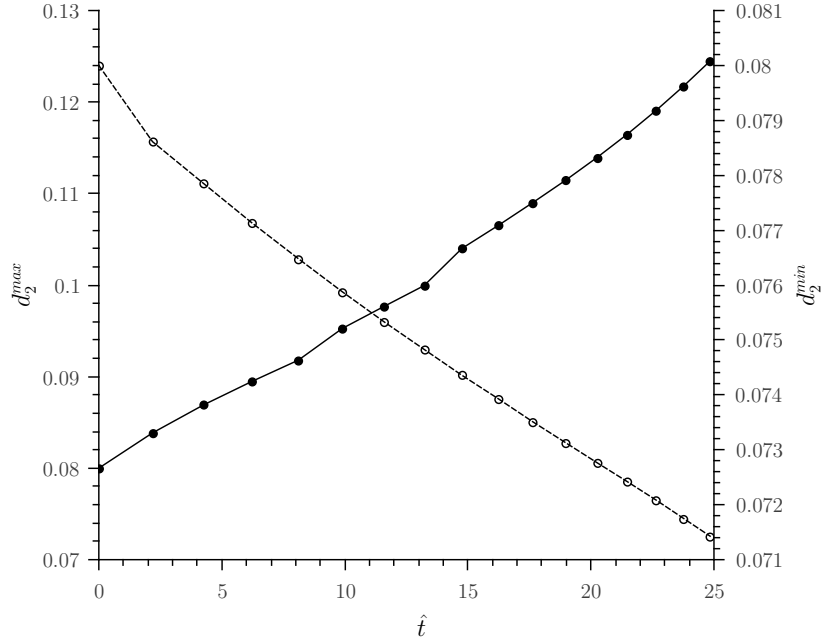


Figure 4. Time evolution of the minimum (dashed line-right axis) and maximum (solid line-left axis) SI thickness for the model of fig. 2c.

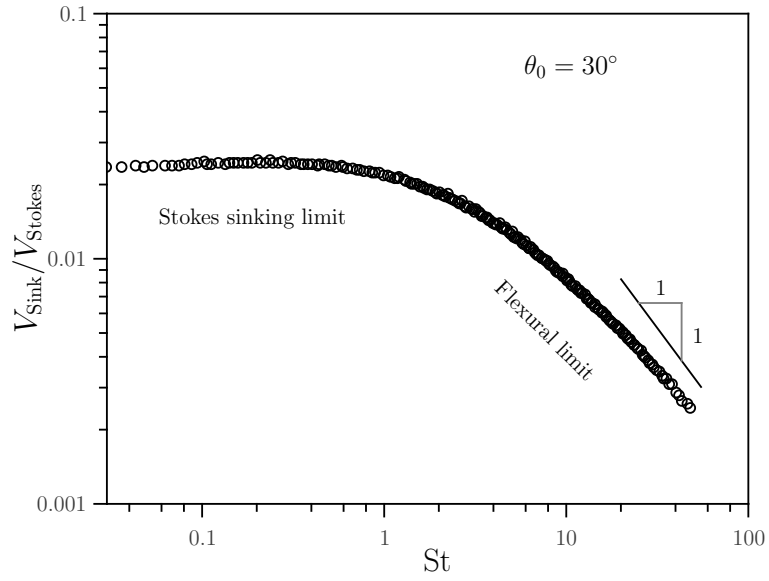


Figure 5. Dimensionless sinking speed $V_{\text{Sink}}/V_{\text{Stokes}}$ as a function of the plate stiffness St for $\theta_0 = 30^\circ$. Numerical solutions were obtained for $L_{\text{SP}}/h_{\text{SP}}=16$, $d_1/h_{\text{SP}} \in [0.1, 0.2]$, $\ell/h_{\text{SP}} \in [5, 10]$, and $\lambda_1 \in [50, 10^5]$. As demonstrated in Ribe [2010], the only effect of the lubrication layer thickness d_1 is to modify ℓ_b , hence the flexural stiffness St .

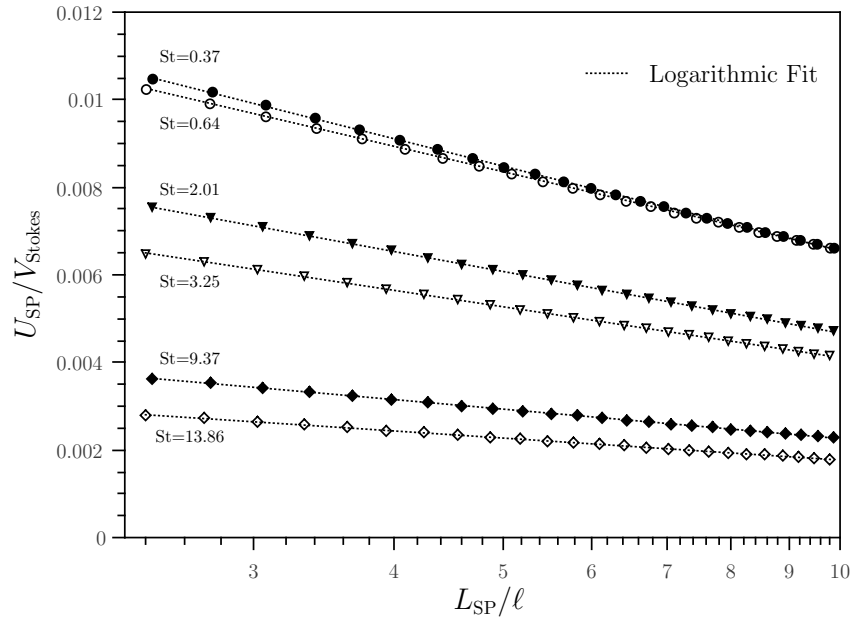


Figure 6. Dimensionless plate speed $U_{\text{SP}}/V_{\text{Stokes}}$ as a function of L_{SP}/ℓ for several values of St and $\theta_0 = 30^\circ$ (semi-log plot). Values of $St \in [0.37, 14]$ were obtained using the following parameters: $\ell/h=7$ (\bullet , \blacktriangledown , \blacklozenge), $\ell/h=5$ (\circ , \triangledown , \diamond) and $\lambda=10^2$ (\bullet , \circ), $\lambda=10^3$ (\blacktriangledown , \triangledown), $\lambda=10^4$ (\blacklozenge , \diamond).

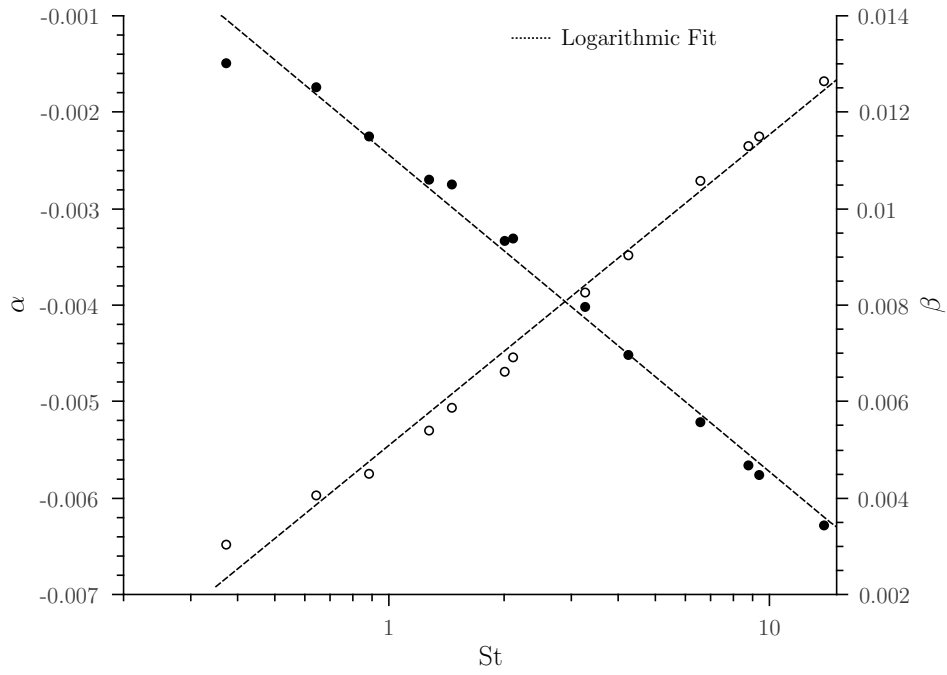


Figure 7. Values of the slope (left y-axis, open circles) and the intercept (right y-axis, solid circles) extrapolated from the logarithmic fit of curves $U_{SP}/V_{Stokes} = fct(L_{SP}/\ell)$ like the ones shown in figure 6. St varies within the range $\sim [0.3-14]$.

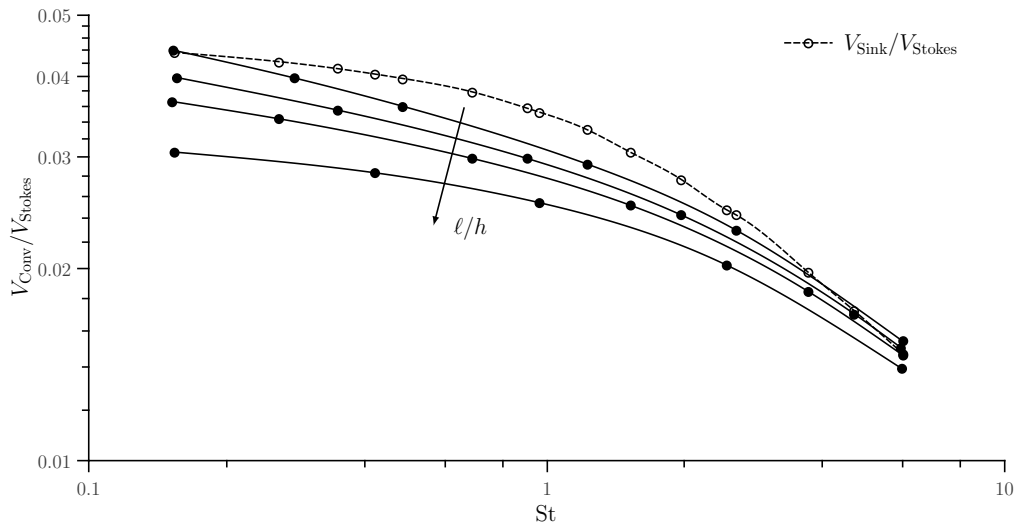


Figure 8. Dimensionless convergence speed V_{Conv}/V_{Stokes} as a function of the flexural stiffness St for $\ell/h = 5, 6, 7, 9$. The corresponding curve V_{Sink}/V_{Stokes} vs. St is shown for comparison. The slab dip is fixed at $\theta_0 = 60^\circ$.

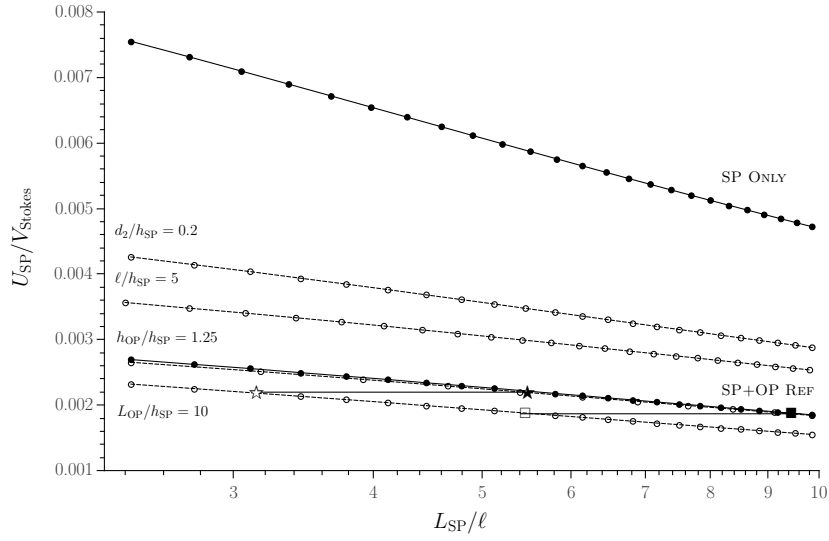


Figure 9. Dimensionless plate speed U_{SP}/V_{Stokes} as a function of L_{SP}/ℓ (semi-log plot) for the SP+OP case. Solid lines: SP ONLY and SP+OP reference cases whose configuration is given in table 3. Dashed lines: variations of the SP+OP reference case with respect to the parameter indicated. $L_{SP}/L_{OP} \approx 2$ along the line (\star, \star), while $L_{SP}/L_{OP} \approx 4$ along the line (\blacksquare, \square).

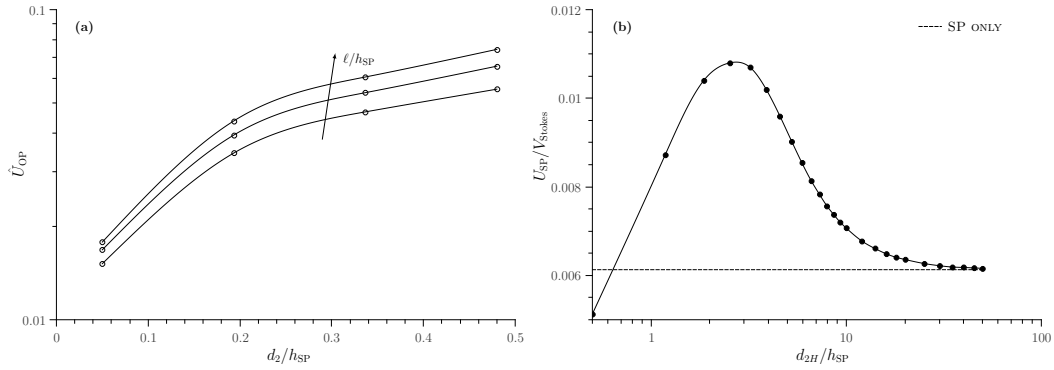


Figure 10. (a) Dimensionless OP speed vs. dimensionless subduction interface thickness d_2/h_{SP} , for $\ell/h_{SP} = 5, 6, 7$. The ratio $L_{SP}/\ell = 3.2$ is constant. The parameters not specified explicitly are given in table 3. (b) Dimensionless plate speed U_{SP}/V_{Stokes} as a function of d_{2H}/h_{SP} for the reference case, where d_{2H} is the horizontal (as opposed to normal) separation between the SP and the OP. The slab length is $\ell/h_{SP} = 5$ and $L_{SP}/\ell = 3$. The other parameters are those given in table 3. The dashed line indicates the value of U_{SP}/V_{Stokes} for the corresponding SP ONLY case.

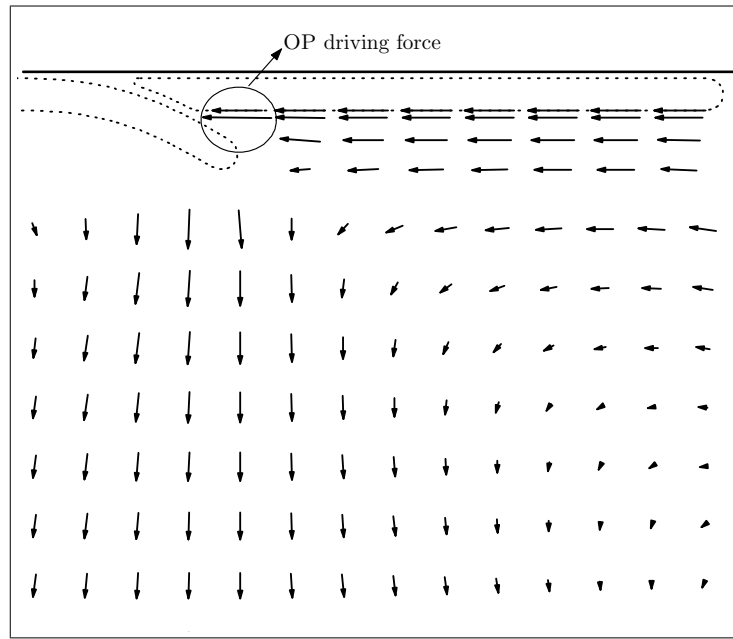


Figure 11. Mantle flow generated by the sinking slab at $t = 0$ for the parameters of table 3. The oval indicates the velocity gradient corresponding to a shear stress that drives the OP leftward.

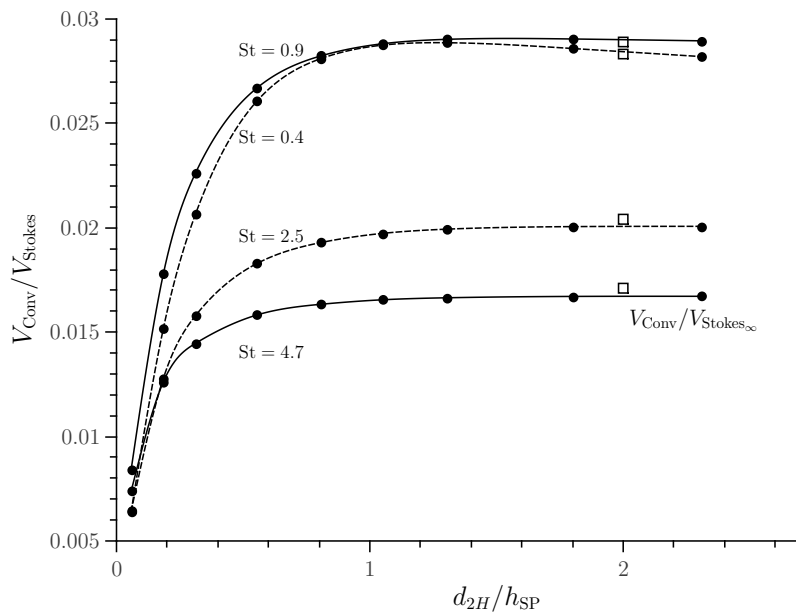


Figure 12. Dimensionless convergence speed $V_{\text{Conv}}/V_{\text{Stokes}}$ vs. dimensionless horizontal SP/OP separation d_{2H}/h_{SP} , for several values of the flexural stiffness St and $\theta_0 = 60^\circ$. The dimensionless slab length $\ell/h_{\text{SP}} = 9$ (dashed lines) or 6 (solid lines). The open squares indicate the values of $V_{\text{Conv}}/V_{\text{Stokes}}$ for the SP ONLY case ($d_{2H}/h_{\text{SP}} \rightarrow \infty$).

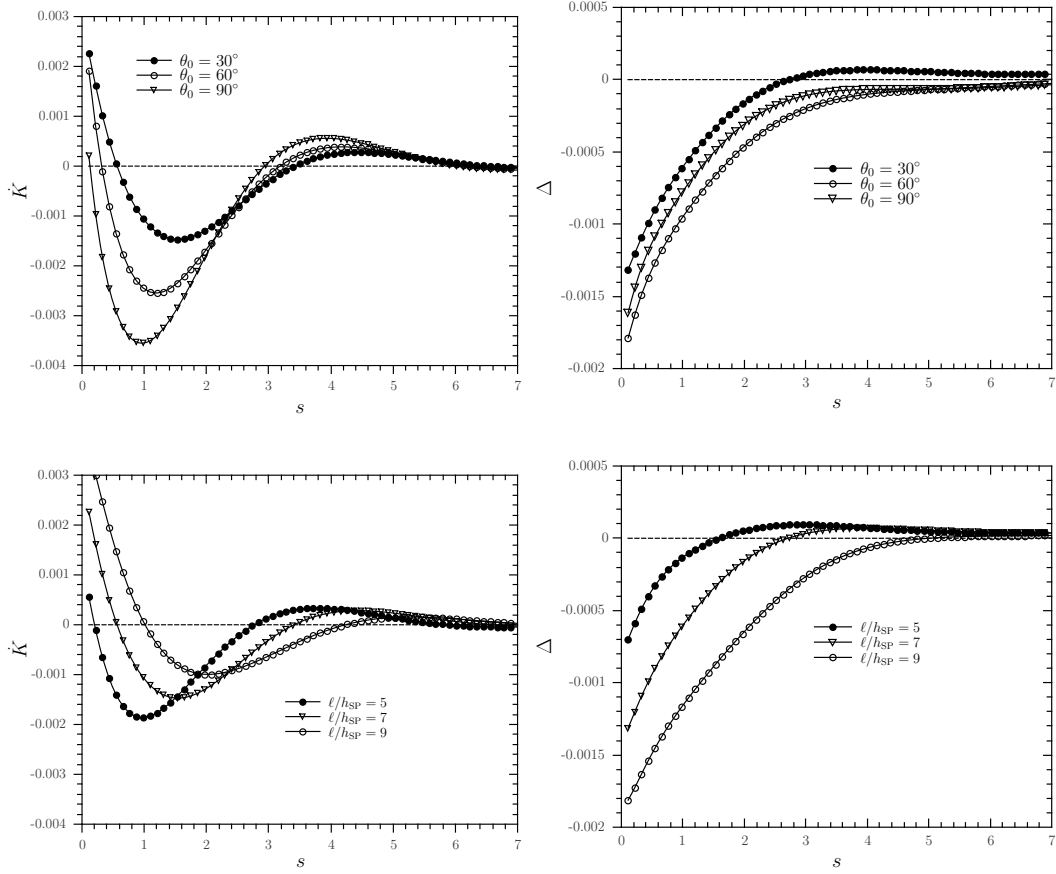


Figure 13. Curling rate K and stretching rate Δ along the midsurface of the OP for three different values of θ_0 , $\ell/h_{SP} = 7$, and $\Gamma = 0$ (top figure) and for three different values of ℓ/h_{SP} , $\theta_0 = 30^\circ$, and $\Gamma = 0$ (bottom figure). The other parameters are given in the text.

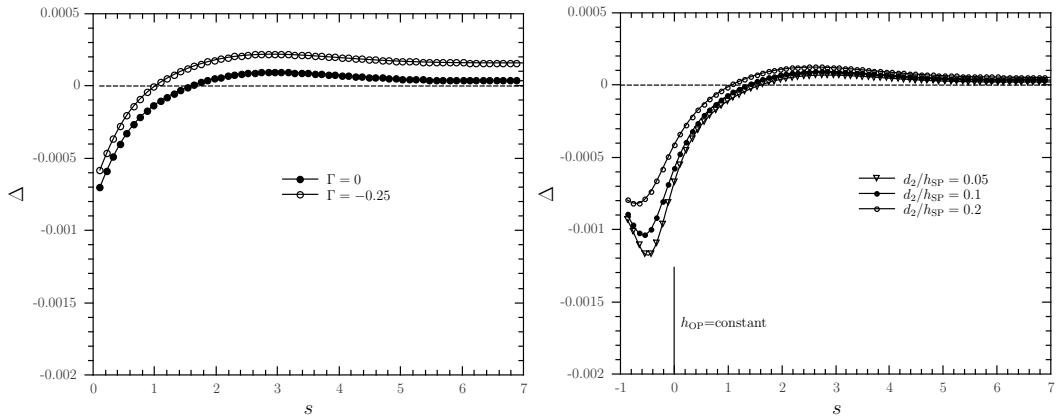


Figure 14. Left figure: stretching rate Δ along the midsurface of a neutrally buoyant ($\Gamma = 0$) or positively buoyant ($\Gamma = -0.25$) OP. Right figure: Stretching rate Δ for different values of d_2/h_{SP} . Arclengths $-1 \leq s \leq 0$ correspond to a leftward extension of the midsurface into the triangular endpiece of the OP (fig. 1). For both figures $\ell/h_{SP} = 5$ and $\theta_0 = 30^\circ$. The others parameters are given in the text.

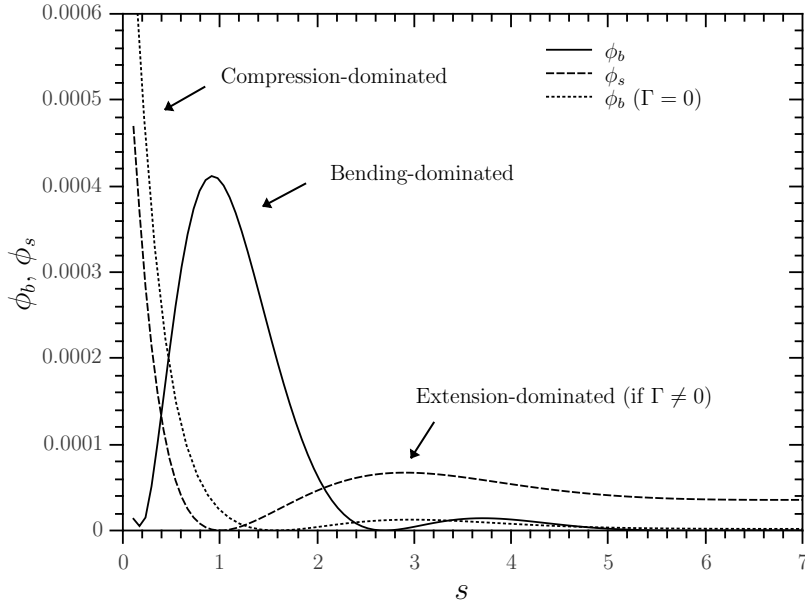


Figure 15. Rates of energy dissipation due to bending (ϕ_b , solid line) and stretching/shortening (ϕ_s , dashed line) of a positively buoyant OP with $\Gamma = -0.25$. For comparison, the dotted line shows the stretching/shortening curve for a neutrally buoyant OP ($\Gamma = 0$).

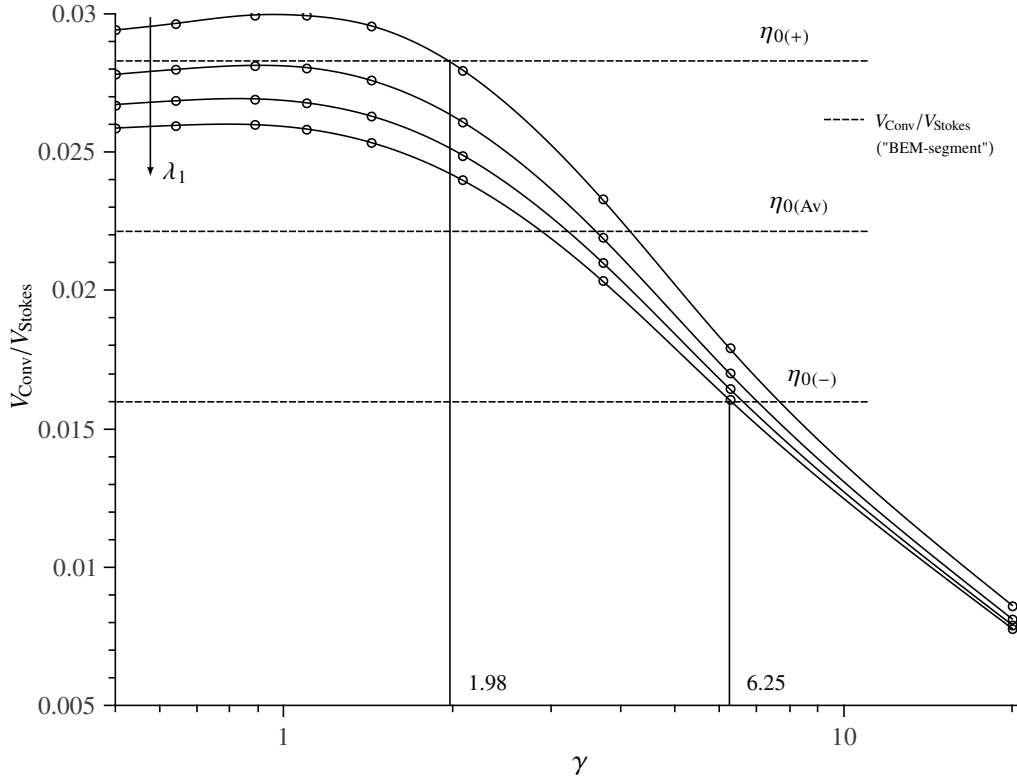


Figure 16. Dimensionless convergence speed plotted against dimensionless interface strength for different values of the viscosity ratio of the plates: $\lambda_1 = 150, 250, 350, 450$. The horizontal dashed lines represent the values of V_{Conv}/V_{Stokes} that correspond to the true convergence rate of the ‘BEM-segment’, nondimensionalized using the range of mantle viscosities given by Mitrovia & Forte [2004]. See text for more details.

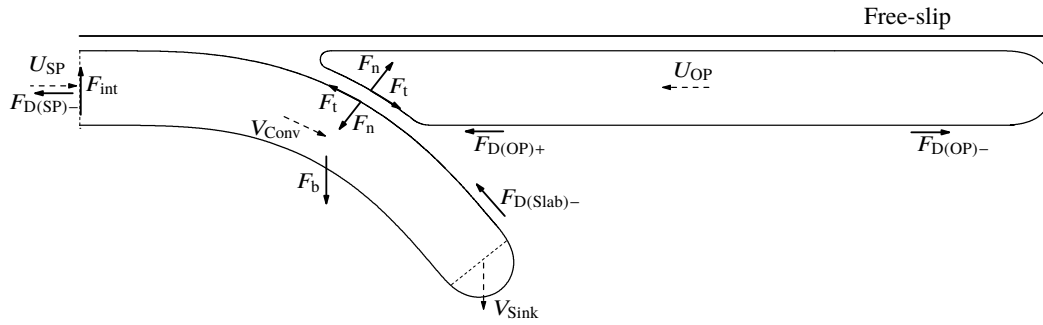


Figure 17. Principal forces and velocities associated with subduction. The dashed lines indicate the characteristic velocities of the two plates, and the thick lines indicate the forces acting on them. $F_{D(OP)+}$ is the drag force driving the OP motion while the different forces $F_{D(xxx)-}$ represent the drag resisting the displacement of the portion of the plate to which they refer. F_n and F_t are the lubrication forces acting on the two plates, equal in magnitude and opposite in direction. F_{int} is the internal force of the SP opposing its bending and F_b is the slab's negative buoyancy driving the entire system. The portion of the SP shown, of length ℓ_b , is the portion where the bending moment is significant.

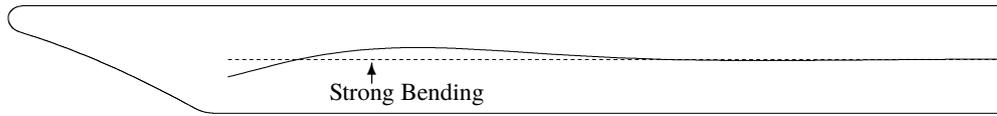


Figure 18. Deformation of the OP midsurface. The dashed line represents the initial shape of the midsurface, while the solid line indicates its new position after one time step. The vertical displacement of the midsurface has been exaggerated by a factor $\sim 10^2$. The model is the case $\ell/h_{SP} = 5$, $\theta_0 = 30^\circ$ shown in fig. 13 (at the bottom).

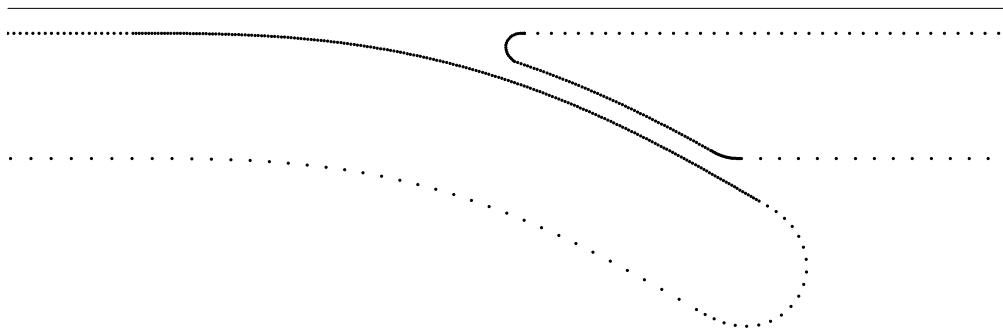


Figure 19. Mesh of the model.